Experimental study of wave diffraction loads on a vertical circular cylinder with heave plates at deep and shallow drafts

Seung-Yoon Han, Benjamin Bouscasse, Vincent Leroy, Sylvain Delacroix, Félicien Bonnefoy, Erin Bachynski-Polić, David Le Touzé

Ocean Engineering 312 (2024) 118970

Contents lists available at ScienceDirect

Ocean Engineering

journal homepage: www.elsevier.com/locate/oceaneng

Research paper

Experimental study of wave diffraction loads on a vertical circular cylinder with heave plates at deep and shallow drafts

Seung-Yoon Han [a,*], Benjamin Bouscasse [a], Vincent Leroy [a], Sylvain Delacroix [a], Félicien Bonnefoy [a], Erin E. Bachynski-Polić [b], David Le Touzé [a]

[a] Nantes Université, École Centrale Nantes, CNRS, LHEEA, UMR 6598, F-44000 Nantes, France
[b] NTNU, Department of Marine Technology, 7491 Trondheim, Norway

ARTICLE INFO

Keywords:
Wave loads
Monochromatic waves
Bichromatic waves
Heave plates
Floating wind turbine
Tank testing

ABSTRACT

This study focuses on wave diffraction loads influenced by heave plates at deep and shallow submerged depths. An extensive experimental campaign is conducted on a fixed vertical and free-surface piercing circular cylinder with five different circular plates, including a perforated plate. The horizontal and vertical wave forces are studied in monochromatic and bichromatic waves. The results show that the heave plate significantly influences the forces varying in time and representative harmonics, including sum- and difference-frequency components. The study found that wave steepness and submerged depth of the plate contribute to the nonlinearity of the loads and that the porous plate reduces the loads compared to the solid plate. Corresponding results from a boundary element method (BEM) solver, HydroStar, provide a reasonable prediction of the harmonics. However, the first harmonic of the vertical force is underpredicted at low frequencies, specifically where the BEM results indicate the cancellation of the forces. Dedicated computational fluid dynamics (CFD) simulations are carried out to investigate the discrepancy, and it is observed that flow separation occurs around the edge of the plate. A simplified approach based on Morison's equation is employed to model the flow separation effects using a quadratic drag force calculated with a constant drag coefficient. The approach shows that viscous drag is the dominant contributor to vertical wave forces on the heave plate in the low-frequency regime.

1. Introduction

Predicting wave loads exerted on a floating wind turbine (FWT) is necessary for the design of substructures, mooring lines, and power cables. The loads significantly influence dynamic responses of the FWT system, potentially leading to extreme responses, drift motions, and vibrations due to system resonance. Therefore, accurately evaluating the wave loads acting on FWTs is crucial for designing systems that can operate robustly for production in harsh offshore environments throughout their design life.

Installing a heave plate is a practical solution to reduce the responses of the floating system. In particular, plates are widely used on semi-submersible floaters (Roddier et al., 2010; Lopez-Pavon et al., 2015; Pegalajar-Jurado et al., 2018; Robertson et al., 2020) as well as in barge-type floaters (Choisnet et al., 2016). The heave plate increases both the hydrodynamic damping of the system and the added mass. The increase in added mass can move the natural frequency out of the wave frequency range. These attributes have been confirmed through numerous experimental and numerical studies (e.g. Tao and Thiagarajan (2003a,b)), focusing on the motion-induced hydrodynamic loads represented by the added mass and damping. Although this well-established knowledge has been handed on to the floating wind communities, further investigation is still needed regarding the effects of the heave plate on wave loads, especially for configurations that are relevant for FWTs.

The wave loads in ocean engineering are commonly categorized into three different frequency regimes (DNV-RP-C205, 2010): wave frequency (WF), low frequency (LF), and high frequency (HF). The dominant contribution to the wave loads comes from the wave frequency regime, where the waves carry most of their energy. Accordingly, the design of the FWT systems aims to avoid having their natural frequencies fall within the wave frequency range by adjusting their natural frequencies to be lower or higher than the wave frequencies.

Nonlinear wave-wave and wave-body interactions result in low- and high-frequency wave loads, which become more prominent with higher wave nonlinearity. Although the wave loads at low and high-frequency regimes are comparatively smaller than those at the wave frequency regime, they are still critical factors to consider in engineering, such as

* Corresponding author.
E-mail address: seung-yoon.han@ec-nantes.fr (S.-Y. Han).

https://doi.org/10.1016/j.oceaneng.2024.118970
Received 29 February 2024; Received in revised form 16 July 2024; Accepted 8 August 2024
Available online 24 August 2024

station-keeping and fatigue assessment, because of their ability to trigger resonant behavior. Specifically, the low-frequency wave loads are known as “mean drift loads” or “slowly varying drift loads”, which can cause significant horizontal and vertical motions of moored structures. On the other hand, the high-frequency wave loads can excite high-frequency resonant responses of stiff systems (e.g., tendons of tension leg platforms), commonly referred to as “ringing” in the transient state and “springing” in the steady state as described in Molin (2023).

The wave loads on a fixed body can be evaluated using a diffraction theory based on the potential flow hypothesis. This diffraction approach does not take into account the contribution of the motion response to the wave load. The loads are decomposed into the zeroth-, first-, second-, and higher-order components by using the perturbation series with respect to the wave steepness parameter ($\varepsilon = k_0 A$ with wavenumber, k_0, and wave amplitude, A).

Analytical solutions can be found for a fixed vertical circular cylinder. For the first-order wave loads, McCamy and Fuchs (1954) and Garrett (1971) solved the linear diffraction problem on bottom-mounted and truncated cylinders. The theory was extended by Kim and Yue (1989) to the pure second-order wave loads on the truncated cylinder in regular waves. Kim and Yue (1990) presented the second-order sum- and difference-frequency loads using an interaction of two wave frequency components called bichromatic waves. Furthermore, Malenica and Molin (1995) presented a complete third-order wave load theory on the bottom-mounted vertical cylinder to investigate the ringing phenomenon. Faltinsen et al. (1995) introduced the FNV (Faltinsen, Newman and Vinje) method to compute the higher-order wave loads.

Dedicated wave tank testing campaigns were conducted to study the linear and nonlinear wave loads acting on a fixed model in regular waves with angular frequency $\omega = 2\pi/T$ where T is the wave period. The loads measured by a force transducer are interpreted using Fourier analysis, resulting in obtaining the harmonic components (0th, ω, 2ω, 3ω, …) and compared with the corresponding order of nonlinearity from the potential flow theory. For instance, Mavrakos and Grigoropoulos (1994) presented the horizontal wave forces and moments on a truncated cylinder obtained using Fast Fourier Transform (FFT). The higher harmonics of the wave loads (up to the fifth harmonic) obtained by the Fourier transform were reported by Boo (2006) for the truncated cylinder and by Kristiansen and Faltinsen (2017) for the bottom-mounted cylinder. Both considered various wave steepnesses and compared the harmonics with the corresponding orders computed by the FNV method.

Besides, the slowly varying drift forces, which are in the low-frequency regime, can also be measured by generating the bichromatic waves in the wave tank. Fonseca et al. (2011) carried out experiments with a fixed buoy in monochromatic and bichromatic waves. The wave loads were reported as the first harmonics of two wave components (ω_1, ω_2) as well as the difference frequency component, $|\omega_1 - \omega_2|$. The harmonic components were obtained by the standard Fourier analysis as well as by the least-square methods using the second harmonic approximation.

These theoretical and experimental methods have been extensively used in many applications to estimate the wave loads acting on floating wind turbines. In particular, numerous engineering models are time-domain solvers relying on a hydrodynamic database calculated using linear potential flow theory. However, engineering models have difficulties in modeling the heave plate of a floater and often require calibration of hydrodynamic coefficients based on experimental data or computational fluid dynamic (CFD) simulations. Despite these efforts, the models tend to underpredict the nonlinear wave loads, as reported in Lopez-Pavon et al. (2015), Simos et al. (2018), Robertson et al. (2017, 2020), Robertson and Wang (2021), Fonseca et al. (2022). Therefore, further research is needed to understand better the wave loads on floating wind turbines equipped with heave plates.

This wave diffraction study aims to experimentally investigate the effect of heave plates on wave diffraction loads and provide as comprehensive an understanding as possible of the domain of validity of engineering models. A fixed vertical and surface-piercing cylinder is studied with and without a circular plate. Five heave-plate configurations, including porosity with varying diameters and a constant plate thickness, are tested with two submerged depths. Two types of long-crested waves, monochromatic and bichromatic waves, are used to investigate the influence of heave plates on wave loads in the different frequency regimes. The detail of the experimental setup and wave test parameters, defined by the wave amplitudes and frequencies, is described in the following Section 2.

Section 3 introduces boundary element methods (BEMs) based on potential flow theory, used as a support for the experimental campaign. Heave plate modeling is addressed using source and dipole methods, particularly for thin plates. The computations of linear and nonlinear wave diffraction loads are briefly outlined in collaboration with numerical schemes. Section 4 presents experimental data analysis, examining force time series and harmonic content using FFT for all configurations. The measured wave loads are approximated with harmonic components obtained from monochromatic and bichromatic waves. The correspondence between the measured wave loads and theoretical computation is also presented in this section. The results are provided in Section 5. The effects of heave plates on wave loads are investigated with respect to the wave steepnesses, submerged depths, and porosity. The harmonic content of experimental measurements is systematically compared with the corresponding order from the potential flow theory.

Detailed discussion is made in Section 6. The consistency of the present study is first shown on a solitary vertical circular cylinder by comparison with the existing literature. Further investigation employs an incompressible Navier–Stokes (CFD) solver to numerically visualize the flow field around the heave plate, particularly flow separations. A simplified Morison equation is used to model the flow separation as the viscous drag forces. Additionally, we discuss the determination of the drag coefficients for different wave steepness and plate diameters. As a result, this section identifies three different vertical wave force regimes based on experimental and numerical investigation. Finally, the conclusions are given in Section 7.

2. Experimental setup

The experiments are carried out in the hydrodynamic and ocean engineering tank of Ecole Centrale Nantes (see Fig. 1). The main dimensions of the tank are 48.4 m in length, 30.0 m in width, and 5 m in water depth h. The tank is equipped with a flap-type wave maker (composed of 48 flaps mounted on a hinge) to generate the waves and an absorbing beach with 9.7 m of length to reduce the reflected waves. The wave maker can generate regular waves with periods from 0.5 s to 5.0 s, and the maximum wave height is limited to 1.0 m. A hexapod is utilized to restrain an experimental model mounted on a tripod installed in the middle of the tank. The model is located 17.2 m away from the wave maker in a longitudinal direction and 15.0 m away from each side of the tank.

This study examines two types of waves: monochromatic and bichromatic waves. The monochromatic waves, also known as “regular waves”, allow us to measure the loads in different harmonics excited by a single wave frequency, ω. On the other hand, the bichromatic waves are composed of two sets of regular waves (ω_1 and ω_2) designed to obtain the loads occurring at a sum frequency ($\omega^+ = \omega_1 + \omega_2$) and difference frequency ($\omega^- = |\omega_1 - \omega_2|$) by using the interaction of two wave components.

2.1. Experimental model

The experimental model is designed as a single vertical circular cylinder with a circular heave plate attached at the bottom to minimize interference caused by any geometrical complexity. This model has three main components, as illustrated in Fig. 2(a): an outer cylinder shell, base plate, and heave plate. The cylinder shell and heave plate

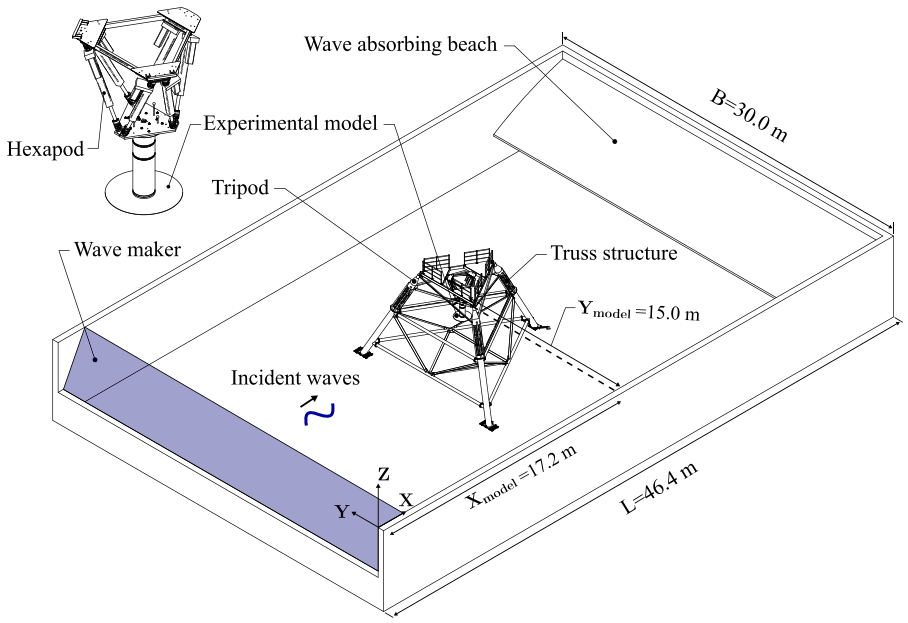

Fig. 1. Experimental setup and incident waves propagating in positive x-direction in the ocean engineering tank at Ecole Centrale Nantes.

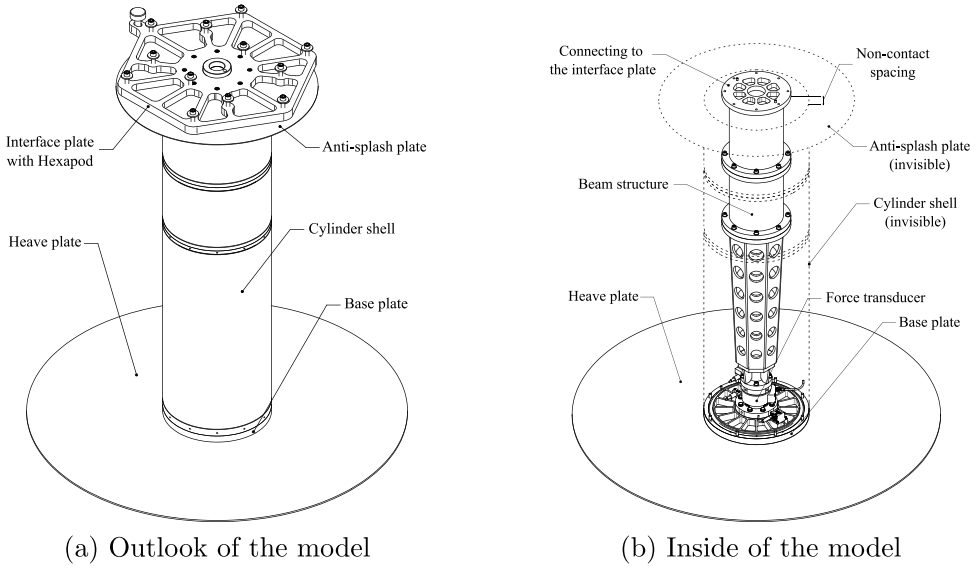

Fig. 2. General arrangement of the experimental model and beam structure.

are directly connected to the base plate to facilitate the change of heave plate configurations.

Fig. 2(b) illustrates the internal structure of the model. The base plate of the model is linked to a rigid beam structure through a force transducer. The beam structure is mounted on the hexapod using an interface plate. This arrangement enables measurement of the total load exerted on the cylinder and plate. Moreover, the shell and beam structures can be separated into three smaller parts to adjust the draft easily. All parts are well-connected and completely waterproof, ensuring the safety of the sensors located inside the cylinder. The model installed on the hexapod is shown in Fig. 4.

Five plate configurations are selected, represented by the cylinder diameter D_c and plate diameter D_d (see Fig. 3). The plate diameter ratios (D_d/D_c) are adapted from real FWT projects, mostly semi-submersibles: e.g. Floatgen (Choisnet et al., 2016), DeepCwind (Robertson et al., 2020), HiPRWind (Lopez-Pavon et al., 2015), and WindFloat platform (Roddier et al., 2010). In addition, a porous plate with porosity ratio $\tau = 10\%$ is considered for the diameter ratio, $D_d/D_c = 2.9$. The plate thickness t_d is 5 mm for all configurations. The effect of plate aspect ratio (t_d/D_d) is not considered, as the plate is thin for all configurations. Furthermore, deep ($d/D_c = 2.2$), and shallow ($d/D_c = 0.7$) drafts are examined to investigate the free surface effects where d is the submerged depth of the model. The main dimensions of the model are given in Table 1.

The heave plate is made of stainless steel to provide sufficient stiffness, while the other parts of the model are made of aluminum. Natural frequencies of the model are measured in both dry and wet conditions using hammer tests conducted inside and outside the wave tank. Each configuration has different natural frequencies due to variations in total mass and the plate's diameter. Multiple modes are observed, particularly because of the plate. The wet mode generally appears at a lower frequency than the dry mode due to the added mass of the fluid. Additionally, the frequency at the deep draft is slightly lower than at the shallow draft. Therefore, the lowest natural frequency is observed at around 5 Hz for the largest plate ($D_d/D_c = 3.5$) at the deep draft ($d/D_c = 2.2$). This value serves as a reference for the signal processing.

(a) $D_d/D_c = 1.0$ (b) $D_d/D_c = 1.5$ (c) $D_d/D_c = 2.9$ (d) $D_d/D_c = 2.9(\tau)$ (e) $D_d/D_c = 3.5$

Fig. 3. A truncated circular cylinder with various heave plates mounted at the bottom of the cylinder including a solitary cylinder ($D_d/D_c = 1.0$).

Table 1
Dimensions of experimental models: the truncated circular cylinder with and without heave plates.

Parameter	Unit	Model A	Model B	Model C	Model D	Model E
D_c	m	0.35	0.35	0.35	0.35	0.35
D_d	m	0.35	0.53	1.00	1.00	1.23
t_d	m	0.005	0.005	0.005	0.005	0.005
d	m	0.775, 0.250	0.775, 0.250	0.775, 0.250	0.775, 0.250	0.775, 0.250
τ	–	0.0	0.0	0.0	0.1	0.0
D_d/D_c	–	1.0	1.5	2.9	2.9	3.5
d/D_c	–	2.2, 0.7	2.2, 0.7	2.2, 0.7	2.2, 0.7	2.2, 0.7
Note	–	Truncated cylinder		Cylinder with heave plate		

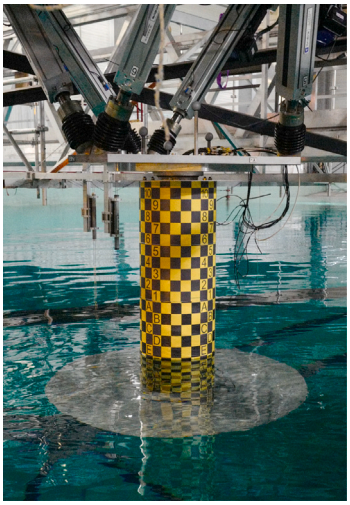

Fig. 4. Picture of the truncated circular cylinder with the heave plate ($D_d/D_c = 3.5$) mounted on the hexapod in the wave tank.

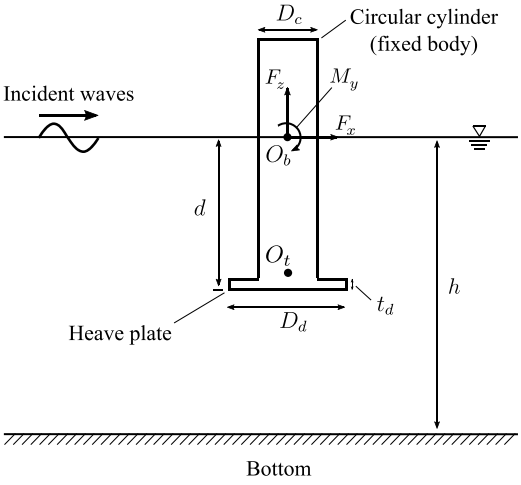

Fig. 5. Load convention for the fixed body in the wave tank: F_x, F_z, M_y stand for the measured forces and moments at the origin of the body-fixed reference, O_b, converted from the ones measured by force transducer at O_t.

2.2. Instrumentation

This study focuses on wave loads exerted on the cylinder and the plate. A six-component force transducer (HBM: MSC10-BG2) is installed between the heave plate and the beam structure. The nominal forces of the transducer are 2 kN for F_x and 10 kN for F_z, with linearity deviation and relative hysteresis less than 0.03% of sensitivity computed based on ITTC (2002). The data is acquired at a sampling rate of 200 Hz. The loads measured by the transducer include the gravity loads $\overline{F}^{(W)} = m\mathbf{g}$ (where m is the model's mass and $\mathbf{g}$ is the acceleration due to gravity), the hydrostatic buoyancy at rest $\overline{F}^{(S)}$, and the wave-induced loads. The inertia loads do not contribute to the measured loads since the hexapod firmly restricts body motions. Therefore, the wave loads, hereafter referred to as $\mathbf{F}$, are obtained by subtracting the buoyancy and weight contributions from the measured loads. These unbalanced forces are eliminated from the measurements during the zeroing process, along with the initial offset of the sensor.

Fig. 5 presents the load convention expressed in the body-fixed reference frame $\{b\}$, which is identical to the Galilean reference frame $\{O\}$ for the fixed body. The forces and moments measured by the transducer at O_t are converted to the ones at the origin of the reference system, O_b, located on the free surface. The z-axis of the reference frame is aligned with the cylinder axis and points upward in the positive direction. Additionally, the x-axis is aligned with the wave direction.

2.3. Test conditions

One single vertical cylinder is tested with all heave plate configurations in two immersed drafts: deep ($d/D_c = 2.2$) and shallow ($d/D_c = 0.7$). Two types of long-crested waves (monochromatic and bichromatic waves) are generated by the wave maker in a single wave direction of the positive x-axis.

For the monochromatic wave test, the regular wave periods T are selected from 0.9 s to 3.0 s, which is under the operation limitation of the wave maker. The periods correspond to a non-dimensional wave frequency, $\omega^2 D_c/g$ ranging from 0.2 to 1.7. Furthermore, three wave steepnesses ($H/\lambda = 0.02, 0.04, 0.06$, where H and λ stand for wave height and wavelength) are chosen to investigate the nonlinear effects on the wave loads. Table 2 presents the selected regular wave parameters, including the wave scatter parameter ($\pi D_c/\lambda$) and the Keulegan–Carpenter numbers given by $KC = \pi H/D_c$. Fig. 6 presents an example of a wave field around the cylinder equipped with the largest

Table 2
Monochromatic waves with three wave steepness.

$\omega^2 D_c/g$	$H/\lambda = 0.02$			$H/\lambda = 0.04$			$H/\lambda = 0.06$		
	$\pi D_c/\lambda$	H/D_c	KC	$\pi D_c/\lambda$	H/D_c	KC	$\pi D_c/\lambda$	H/D_c	KC
1.74	0.87	0.07	0.22	0.86	0.15	0.46	0.84	0.22	0.68
1.41	0.70	0.09	0.28	0.69	0.18	0.56	0.68	0.27	0.84
1.16	0.58	0.11	0.34	0.57	0.22	0.68	0.56	0.32	1.02
0.98	0.49	0.13	0.40	0.48	0.26	0.81	0.47	0.39	1.21
0.83	0.42	0.15	0.48	0.41	0.31	0.99	0.40	0.45	1.42
0.63	0.31	0.20	0.63	0.31	0.40	1.26	0.30	0.60	1.89
0.35	0.18	0.34	1.08	0.17	0.71	2.24	0.17	1.07	3.36
0.16	0.08	0.80	2.51	0.08	1.57	4.94			

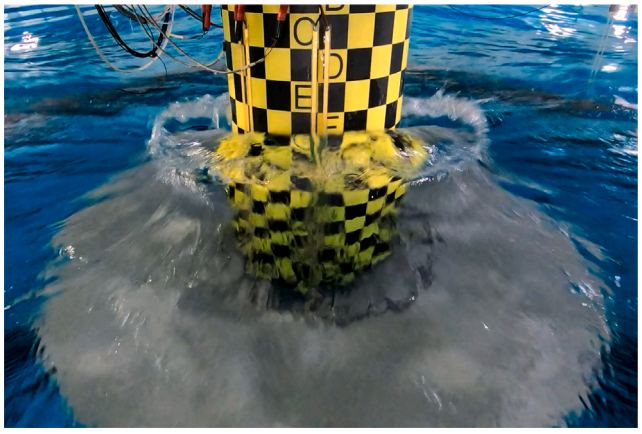

Fig. 6. A snapshot of the diffracted waves around the truncated cylinder with the heave plate ($D_d/D_c = 3.5$) at the shallow submerged depth ($d/D_c = 0.7$, $d = 0.25$ m). A regular wave ($\omega^2 D_c/g = 0.35$, $H/\lambda = 0.04$) propagates from the front to the back.

heave plate ($D_d/D_c = 3.5$) at the shallow draft ($d/D_c = 0.7$) in a regular wave ($\omega^2 D_c/g = 0.4$, $H/\lambda = 0.04$). A video is available in Appendix A.

All the wave steepnesses are examined at the deep draft with the solitary cylinder (Model A) and the cylinder with the single plate (Model C). Only one wave steepness ($H/\lambda = 0.06$) is considered for the other configurations. On the other hand, at the shallow draft, all the steepnesses are tested for all the configurations. However, some wave frequencies could not be tested with the plate due to the large wave amplitude with $H/\lambda = 0.04$ and 0.06.

The regular waves are first calibrated in the tank without the model. A reference wave gauge is installed at the target position $x_{target} = 17.2$ m. An amplification factor is used to calibrate the waves to ensure that the generated waves reach the target wave heights within a range of 5% error. These factors depend on the wave frequency and height and aim to correct the small deviation of the wavemaker linear transfer function. The measured wave heights, including all nonlinearities, are used to non-dimensionalize the results.

The heave plate effects on the slowly varying drift loads are studied using bichromatic waves with the solitary cylinder (Model A) and the heave plate (Model C). Three primary wave frequencies ω_1 are selected from the monochromatic waves, and the secondary wave frequencies ω_2 are set to have a difference frequency $\omega^- = 1.2$ rad/s, which corresponds to $\lambda_{\omega^-}/D_c \approx 124$ assuming deep water. The wave steepness of each wave component in bichromatic waves is designed to be 0.02, which corresponds to the one in the monochromatic waves.

The same amplification factors obtained from the regular wave calibration are used to generate bichromatic waves. The bichromatic waves are generated without the model, and the wave elevation is measured at the target position. In contrast to the regular waves, the individual wave heights cannot be measured. Hence, the measured first-harmonic amplitude, A_j of each wave frequency (ω_j), is used for non-dimensionalization. The test parameters of bichromatic waves are given in Table 3.

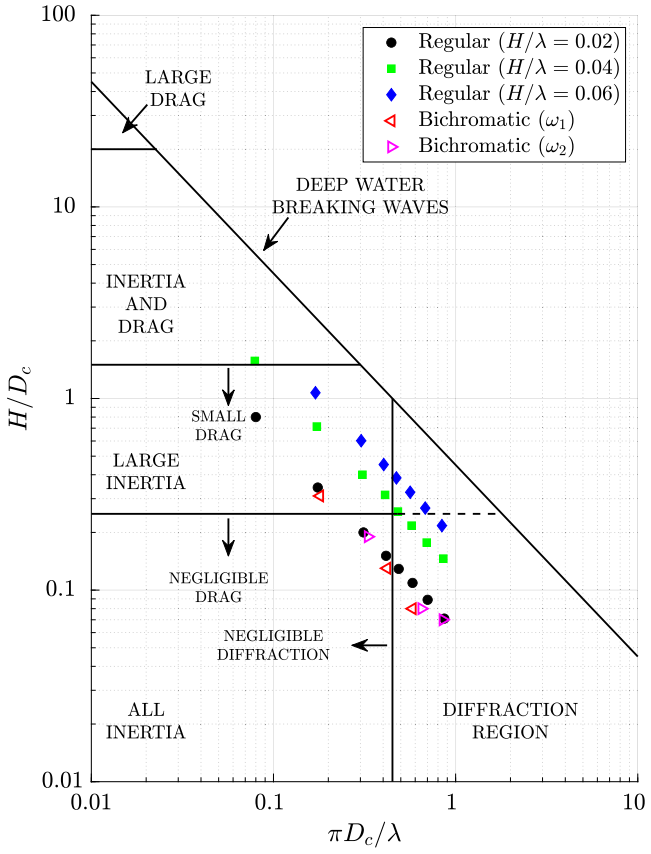

Fig. 7. Monochromatic and bichromatic wave conditions in difference wave force regimes (Chakrabarti, 1987).

Fig. 7 summarizes the wave conditions of the monochromatic waves (symbols with face colors) and bichromatic waves (symbols without face colors). The selected wave conditions are designed to investigate the different wave force regimes introduced by Chakrabarti (1987), including the diffraction, inertia, and drag force regimes. All the waves are below the wave-breaking criteria. The wave components of the bichromatic waves are in a similar frequency range as the monochromatic waves.

3. Numerical model

This section presents a numerical model to evaluate the wave loads on the truncated cylinder with the heave plates used in the experimental study. Perfect fluid (inviscid and incompressible fluid) and irrotational flow assumptions are employed, where the flow can be described by a velocity potential, $\Phi(\mathbf{x}, t)$. In the boundary value problems (BVPs), the whole fluid domain is governed by the Laplace equation ($\nabla^2 \Phi = 0$). The velocity potential satisfies the boundary

Table 3
Bichromatic waves with a difference frequency $\omega^- = 1.2$ rad/s.

Primary wave component (ω_1)				Secondary wave component (ω_2)			
$\omega_1^2 D_c/g$	$\pi D_c/\lambda$	H_1/D_c[a]	KC	$\omega_2^2 D_c/g$	$\pi D_c/\lambda$	H_2/D_c[a]	KC
0.35	0.18	0.31	0.99	0.67	0.33	0.19	0.59
0.83	0.42	0.13	0.41	1.30	0.65	0.08	0.24
1.16	0.58	0.08	0.25	1.70	0.85	0.07	0.21

[a] $H_1 = 2 \times A_1$, $H_2 = 2 \times A_2$.

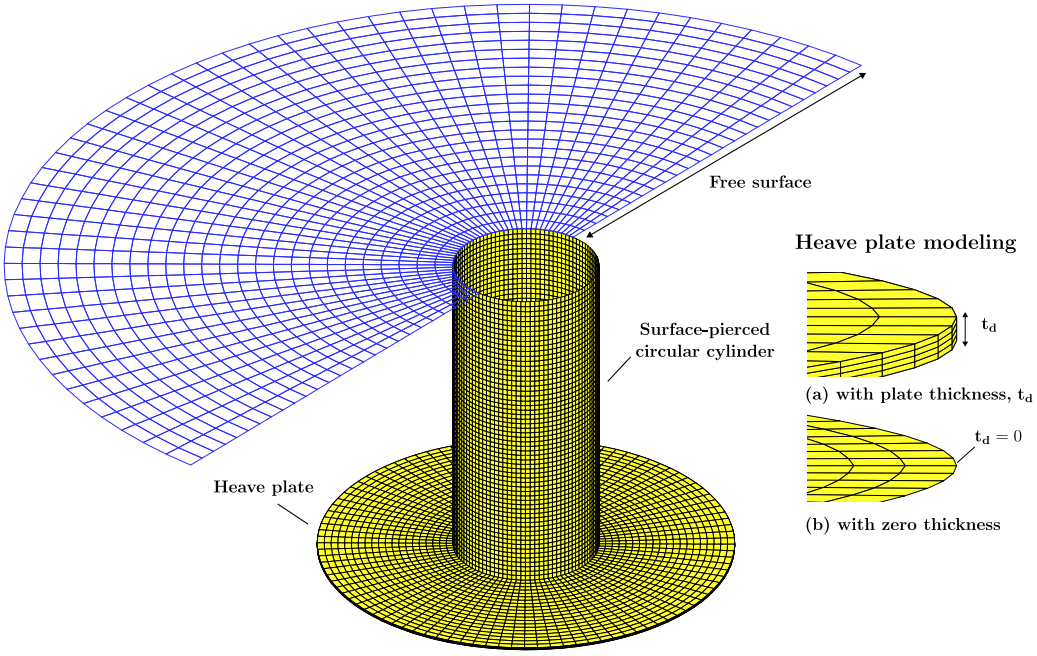

Fig. 8. Discretization of a truncated circular cylinder with a heave plate surrounded by a free surface for the first- and second-order computations in boundary element method: body (yellow), free surface (blue). Heave plate modeling is given with plate thickness, t_d (a), and zero-thickness (b) for source and dipole distribution methods.

conditions on the free surface, bottom, body surface, and radiation conditions. The boundary conditions are developed using Taylor series expansions suggested by Stokes and a perturbation series for the potential at corresponding orders (see, Malenica and Molin (1995)).

A commercial software, HydroStar (Bureau Veritas, 2020), is utilized to solve the BVPs for the first- and second-order problems. The software discretizes the boundary with panels to solve boundary integral equations with a free surface Green function, known as the panel method. A single wave direction is considered in the positive x direction.

3.1. Modeling the heave plates

In the panel method, heave plates can be modeled either by considering their thickness or assuming zero thickness. For the first case, the panels are modeled on the top, side, and bottom of the plate. A source formulation is used to solve the boundary integral equation by defining the velocity potential as a source distribution. On the other hand, the plate can also be modeled as a zero-thickness plate if the thickness is sufficiently small (thin plate) or the plate has porosity. A direct formulation is used to define the velocity potential by source and dipole distributions. Both the top and bottom of the panel are then considered as wetted surfaces. Furthermore, the porous effect can be modeled using Darcy's law, where the porosity is considered as a pressure drop condition linked to the water particle velocity (Chwang, 1983).

An example of the panel model discretization on the cylinder and the heave plate is given in Fig. 8. In this study, we use the source approach on the solid heave plate by modeling the panels four times smaller than the thickness as illustrated in Fig. 8(a). On the other hand, the porous plate is modeled as a zero-thickness plate (see Fig. 8(b)) to use the direct approach. The free surface is modeled with a radius of $10D_d$ for the second-order computation. For the second-order computation, only the source method is available in HydroStar. Therefore, the second-order loads on the perforated plate cannot be computed in this study.

3.2. Computation of wave loads

In the potential flow theory, the wave loads are mathematically described for the monochromatic and bichromatic wave cases. The loads are evaluated with different orders of magnitude by introducing a perturbation series with respect to the wave steepness parameter ($\varepsilon = k_0 A$) as described in Kim and Yue (1989, 1990), Malenica and Molin (1995).

The wave loads are computed by integrating the pressure on the wetted body surface, S_B.

$$\mathbf{F} = \iint_{S_B} p\mathbf{n} dS \tag{1}$$

where the pressure is from the Bernoulli equation: $p = -\rho g z - \rho \frac{\partial \Phi}{\partial t} - \frac{1}{2}\rho(\nabla\Phi)^2$. In this study, the contribution of radiation potential induced by the body motion is discarded in total velocity potential.

In monochromatic waves, the wave loads are decomposed with the different orders as,

$$\mathbf{F}(t) = \mathbf{F}^{(0)} + \Re\mathfrak{e}\{\mathbf{F}^{(1)} e^{-i\omega t}\} + \overline{\mathbf{F}}^{(2)} + \Re\mathfrak{e}\{\mathbf{F}^{(2)} e^{-2i\omega t}\} + \mathbf{O}(\varepsilon^3) \tag{2}$$

where $\mathbf{F}^{(0)}$ is the hydrostatic force at the rest position, and $\mathbf{F}^{(1)}$, $\overline{\mathbf{F}}^{(2)}$, $\mathbf{F}^{(2)}$ stand for the first-order, second-order mean drift and second-order

double frequency forces, respectively. The mean drift forces can be evaluated using the near-field method (Pinkster and Van Oortmerssen, 1978), far-field method (Maruo, 1960; Newman, 1967), and middle-field method (Chen, 2007). The second-order double frequency loads, $\mathbf{F}^{(2)}$, are dealt with following the bichromatic theory.

Additional terms appear for bichromatic waves due to the interactions of the two wave frequency components.

$$\mathbf{F}(t) = \mathbf{F}^{(0)} + \Re\{\sum_{j=1}^{2} \mathbf{F}^{(1)}_{\omega_j} e^{-i\omega_j t}\} + \Re \sum_{j=1}^{2}\sum_{l=1}^{2} \{\mathbf{F}^{(2),-}_{(\omega_j,\omega_l)} e^{-i\omega^- t} + \mathbf{F}^{(2),+}_{(\omega_j,\omega_l)} e^{-i\omega^+ t}\} + \mathbf{O}(\varepsilon^3) \tag{3}$$

where $\omega^- = \omega_j - \omega_l$ and $\omega^+ = \omega_j + \omega_l$. Superscripts + and − stand for the sum- and difference-frequency contributions.

The second-order terms in the above Eq. (3) can be written in quadratic form,

$$\mathbf{F}^{(2)}(t) = A_1^2 \bar{\mathbf{f}}^{(2),-}_{(\omega_1,\omega_1)} + A_2^2 \bar{\mathbf{f}}^{(2),-}_{(\omega_2,\omega_2)} + \Re\{2A_1A_2 \mathbf{f}^{(2),-}_{(\omega_1,\omega_2)} e^{-i\omega^- t}\} + \Re\{A_1^2 \mathbf{f}^{(2),+}_{(\omega_1,\omega_1)} e^{-2i\omega_1 t} + A_2^2 \mathbf{f}^{(2),+}_{(\omega_2,\omega_2)} e^{-2i\omega_2 t} + 2A_1A_2 \mathbf{f}^{(2),+}_{(\omega_1,\omega_2)} e^{-i\omega^+ t}\} \tag{4}$$

where $\mathbf{f}^{(2),+}_{(\omega_1,\omega_2)}$, $\mathbf{f}^{(2),-}_{(\omega_1,\omega_2)}$ are Quadratic Transfer Functions (QTFs) for sum- and difference-frequency components. $\bar{\mathbf{f}}^{(2),-}_{(\omega_1,\omega_1)}$, $\bar{\mathbf{f}}^{(2),-}_{(\omega_2,\omega_2)}$ are the mean drift forces in unit wave amplitude from the difference frequency contribution, and $\mathbf{f}^{(2),+}_{(\omega_1,\omega_1)}$, $\mathbf{f}^{(2),+}_{(\omega_2,\omega_2)}$ are the second-order double frequency loads from the sum frequency contribution where $\omega_j = \omega_l$.

4. Analysis of the experimental data

4.1. Signal processing

The measured force time series is filtered out by a low-pass filter using a 4.5 Hz cut-off frequency. The cut-off frequency is lower than the first wet natural frequency of the plate, which was obtained from the hammer tests (e.g., 5 Hz for the largest plate, $D_d/D_c = 3.5$ at the deep draft, $d/D_c = 2.2$). This ensures that we keep the harmonics of interest associated with the wave frequency. For instance, the highest frequency wave is 1.1 Hz ($\omega^2 D_c/g = 1.74$), which allows up to the third harmonic.

The time series is reduced by selecting a time window with an integer number of wave periods, N. The transient period and wave reflection from the wave-absorbing beach are carefully extruded by considering the first wave arriving time and wave returning time at the model location. For example, in monochromatic waves, the window is $30T$ in length for the short wave period, but for the long wave, the window is limited to $5T$ due to the high group velocity. On the other hand, for the bichromatic waves, the length of the time window is chosen as $10T^-$, where $T^- = 2\pi/\omega^-$.

4.2. Wave loads in monochromatic waves

Fig. 9 shows an example of the horizontal and vertical force time series on Model E ($D_d/D_c = 3.5$) at the deep draft with a single wave frequency ($\omega^2 D_c/g = 1.74$) and the wave steepness ($H/\lambda = 0.06$). The measured signal is compared to the filtered signal, where the higher frequency response is discarded above the cut-off frequency. The filtered signals present satisfactory periodicity, specifically exhibiting sinusoidal behavior in the horizontal forces and the secondary peaks in the vertical forces.

Fourier analysis is used to obtain the harmonic content from the raw time history within the selected window (NT), allowing for precise capture of the zeroth harmonic and minimizing energy losses of each harmonic content in the regular waves. The results of FFT clearly show that the wave loads are distributed to the zeroth and higher harmonics of the horizontal and vertical forces. Additional peaks appear in the FFT, which correspond to the wet natural frequencies of the model. The structural response affects the harmonics of the measured loads located near the natural frequencies. However, below the cut-off frequency, these structural contributions are negligible, and this is the limit of our experimental setup. It is worth noting that the first harmonic in the vertical forces is comparable to the second harmonic, which can be observed as the secondary peak in the force time history shown in Fig. 9 (bottom). In general, the first harmonic is the most dominant, and the first four harmonics, including the zeroth harmonic, account for above 95% of the total harmonic amplitudes.

Therefore, the wave loads in monochromatic waves can be approximated by the following equation,

$$\mathbf{F}(t) \approx \overline{\mathbf{F}} + \Re\{\mathbf{F}^{(\omega)} e^{-i\omega t}\} + \Re\{\mathbf{F}^{(2\omega)} e^{-2i\omega t}\} + \Re\{\mathbf{F}^{(3\omega)} e^{-3i\omega t}\} + \mathbf{O}(4\omega) \tag{5}$$

where $\overline{F}$ is the hydrodynamic contributions of the mean loads, so-called mean wave drift loads. $F^{(\omega)}$, $F^{(2\omega)}$, $F^{(3\omega)}$ are corresponding to the first-, second-, and the third-harmonic components of the Fourier series.

4.3. Wave loads in bichromatic waves

In Fig. 10, an example is provided highlighting the difference-frequency contribution in the horizontal and vertical forces acting on Model C ($D_d/D_c = 2.9$) with the bichromatic wave set ($\omega_1^2 D_c/g = 0.83$ and $\omega_2^2 D_c/g = 1.30$) at the shallow draft. In the time series, the interaction between the two wave components can be observed as a beat with the frequency ω^-. The forces are slowly varying in time with the difference frequency, which is called the slowly varying wave drift forces. All the peaks identified from FFT correspond to the interactions of two wave components, as shown in x-axis up to the third interaction (e.g., $3\omega_{1,2}$, $|2\omega_1 \pm \omega_2|$, $|2\omega_2 \pm \omega_1|$), which is comparable with the sum and difference frequency contributions. The minor peaks correspond to higher interactions.

In bichromatic waves, the least squares procedure (Fonseca et al., 2011; Li and Bachynski-Polić, 2021) is utilized to obtain the first and second harmonic components of ω_1, ω_2, as well as the sum- and difference-frequency components (ω^+, ω^-) from the force time series. This method is more convenient than standard Fourier analysis for extracting the harmonic components from the time history in the bichromatic waves, as there is no condition on the length of the time window.

The following equation then approximates the wave loads in the bichromatic waves up to the second interaction of two wave components:

$$\mathbf{F}(t) \approx \overline{\mathbf{F}} + \Re\{\mathbf{F}^{(\omega_1)} e^{-i\omega_1 t}\} + \Re\{\mathbf{F}^{(\omega_2)} e^{-i\omega_2 t}\} + \Re\{\mathbf{F}^{(2\omega_1)} e^{-2i\omega_1 t}\} + \Re\{\mathbf{F}^{(2\omega_2)} e^{-2i\omega_2 t}\} + \Re\{\mathbf{F}^{(\omega^+)} e^{-i\omega^+ t}\} + \Re\{\mathbf{F}^{(\omega^-)} e^{-i\omega^- t}\} \tag{6}$$

where $F^{(\omega^+)}$, $F^{(\omega^-)}$ are the sum- and difference-frequency forces. The harmonic content of interest, i.e. the one present in Eq. (6), is well indicated by the least-squares fitting procedure given in Fig. 10.

4.4. Correspondence of wave loads in theory and experiments

The harmonic components measured in the experiments given in Table 4 correspond to the wave loads evaluated in different orders by the theory. This study mainly focuses on the influence of the heave plate on the mean drift forces, the first and second harmonic forces, and the sum and difference frequency forces. These contributions are dominant to the wave loads and are of interest in engineering applications.

In this study, the QTFs are computed numerically using the commercial BEM solver HydroStar (Bureau Veritas, 2020). The middle-field method (Chen, 2007) is used for the difference frequency components

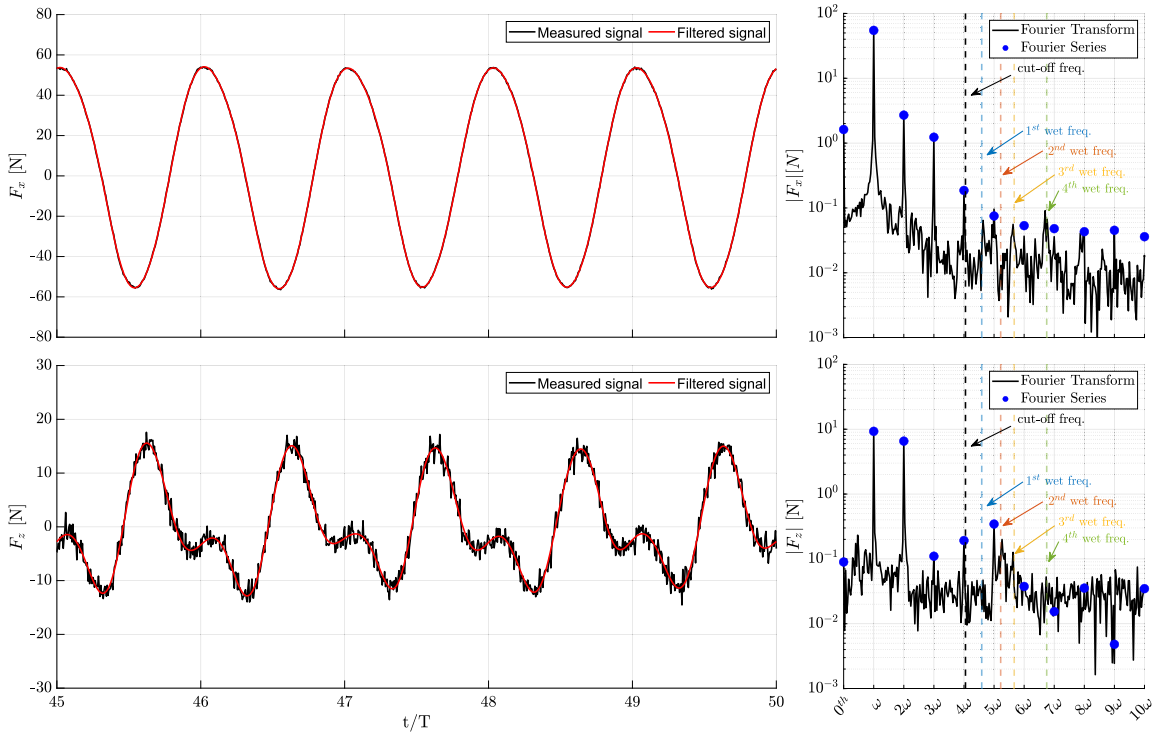

Fig. 9. Time series and harmonic content of horizontal (top) and vertical (bottom) wave forces on a vertical cylinder with the largest plate $D_d/D_c = 3.5$ (with the lowest natural frequency) in monochromatic waves of the non-dimensional wave frequency ($\omega^2 D_c/g = 1.74$) and wave steepness ($H/\lambda = 0.06$) at the deep draft ($d/D_c = 2.2$).

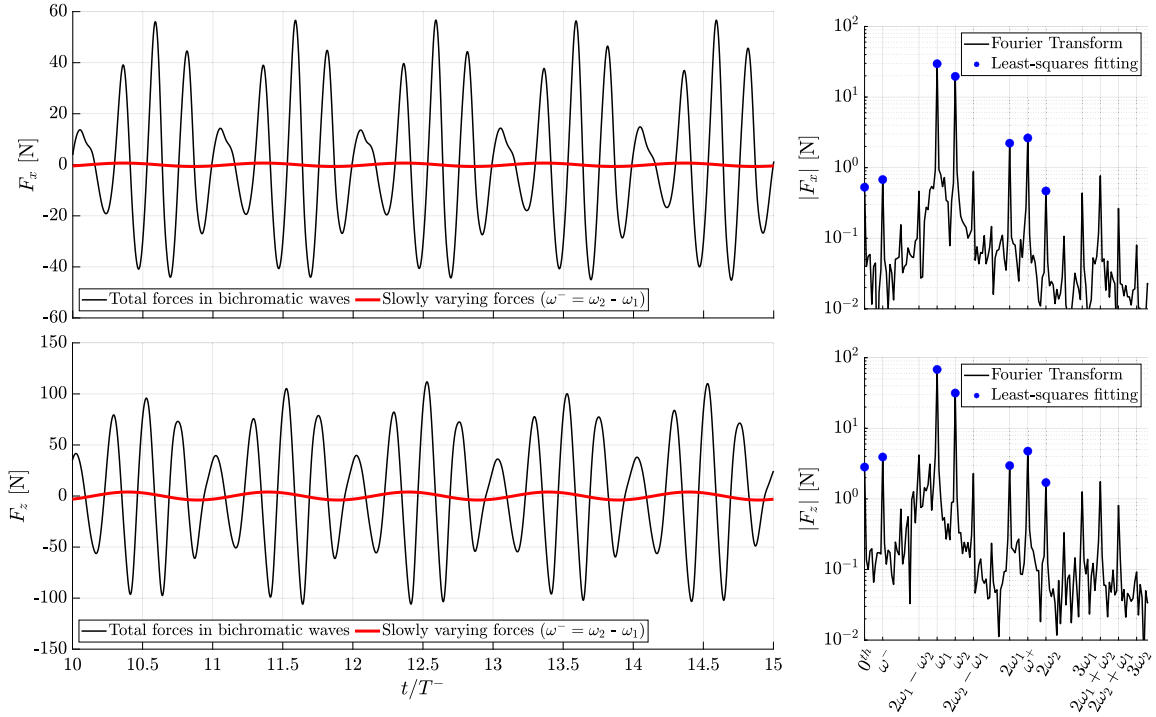

Fig. 10. Time series and harmonic content of horizontal (top) and vertical (bottom) wave forces on a vertical cylinder with a heave plate (Model C, $D_d/D_c = 2.9$) in bichromatic waves ($\omega_1^2 D_c/g = 0.83$ and $\omega_2^2 D_c/g = 1.30$) at the shallow draft ($d/D_c = 0.7$).

to compute the mean drift forces and slowly varying drift forces. The sum-frequency wave loads are computed by the near-field method. The panel models for the cylinder and heave plate are used by following the description in Section 3.2. A constant porous parameter $\kappa = 5$ is employed to implement 10% of porosity of the plate (Model D) for both deep and shallow drafts.

5. Results

5.1. Wave loads in monochromatic waves

This section presents the horizontal and vertical wave loads acting on the cylinder without ($D_d/D_c = 1.0$) and with heave plates ($D_d/D_c =$

Table 4
Correspondence of wave load between harmonics and orders of wave load up to the second interaction of the wave components in the experiment and potential flow theory.

Wave type	Experiments	Harmonics	Theory	Orders ($\varepsilon = k_0 A$)
No waves	$\mathbf{F}^{(W)}$	0th (weight)	–	–
	$\mathbf{F}^{(S)}$	0th (buoyancy)	$\mathbf{F}^{(0)}$	0th
Monochromatic waves	$\overline{\mathbf{F}}$	0th (or mean)	$\overline{\mathbf{F}}^{(2)}$	2nd mean
	$\mathbf{F}^{(\omega)}$	1st	$\mathbf{F}^{(1)}$	1st (linear)
	$\mathbf{F}^{(2\omega)}$	2nd	$\mathbf{F}^{(2)}$	2nd double freq.
Bichromatic waves	$\overline{\mathbf{F}}$	0th (or mean)	$A_1^2\overline{\mathbf{f}}^{(2),-}_{(\omega_1,\omega_1)} + A_2^2\overline{\mathbf{f}}^{(2),-}_{(\omega_2,\omega_2)}$	2nd mean
	$\mathbf{F}^{(\omega)}$	1st of ω_1, ω_2	$\mathbf{F}^{(1)}_{\omega}$	1st (linear)
	$\mathbf{F}^{(2\omega)}$	2nd of ω_1, ω_2	$A^2\mathbf{f}^{(2),+}_{(\omega,\omega)}$	2nd double freq.
	$\mathbf{F}^{(\omega^+)}$	1st at ω^+	$2A_1A_2\mathbf{f}^{(2),+}_{(\omega_1,\omega_2)}$	2nd sum freq.
	$\mathbf{F}^{(\omega^-)}$	1st at ω^-	$2A_1A_2\mathbf{f}^{(2),-}_{(\omega_1,\omega_2)}$	2nd difference freq.

1.5, 2.9, 3.5), including the perforated plate. All results are obtained with regular waves at deep ($d/D_c = 2.2$) and shallow ($d/D_c = 0.7$) drafts. First, the time series of non-dimensional wave loads $F(t)/\rho g D_c^2(H/2)$ is presented together with Fourier series results up to the third harmonics.

Next, the amplitude of the first and second harmonics, as well as the mean value of the forces, are plotted with respect to the non-dimensional wave frequency $\omega^2 D_c/g$ called a harmonic operator. The amplitudes of each harmonic are non-dimensionalized with

$$F'^{(\omega)} = \frac{F^{(\omega)}}{\rho g D_c^2(H/2)}, \qquad F'^{(2\omega)} = \frac{F^{(2\omega)}}{\rho g D_c(H/2)^2}, \qquad \overline{F}' = \frac{\overline{F}}{\rho g D_c(H/2)^2} \tag{7}$$

where superscript indicates the harmonic components, overline stands for the mean value of the forces, and H is the measured wave height of calibrated waves.

Three different wave steepnesses are provided for Model A ($D_d/D_c = 1.0$) and C ($D_d/D_c = 2.9$) at the deep draft and for all configurations at the shallow draft. Each configuration is represented by a different symbol and color. The type of symbol describes the wave steepness (×: $H/\lambda = 0.02$, ○: $H/\lambda = 0.04$, and •: $H/\lambda = 0.06$). The first-, and second-order hydrodynamic loads computed by HydroStar are given in solid lines for comparison.

5.1.1. Time series and harmonic components

One selected time series of wave loads is shown with a single wave component ($\omega^2 D_c/g = 1.0$, $H/\lambda = 0.06$) at deep and shallow drafts. The load time series of all configurations are synchronized and displayed during five wave periods in the periodic state. Furthermore, the Fourier series are obtained using the time series of thirty wave periods.

Fig. 11 presents the horizontal wave forces on the cylinder with all heave plates at deep and shallow drafts. The measured forces show good repeatability in time in general. At the deep draft, the behavior of the horizontal forces in time is almost identical in terms of the amplitudes and phase. However, heave plate effects can be clearly recognized in the Fourier series. Especially the first harmonic of the horizontal force increases with the diameter of the heave plate. Furthermore, the forces with the porous plate are slightly lower than with the equivalent solid plate.

The effect of the heave plate on horizontal forces is more noticeable at shallow draft. In the time series, the positive peaks are higher and sharper with the heave plates, while the phase is shifted compared to the solitary cylinder (Model A). The porosity effects are more noticeable in the time series, reducing the amplitude of the forces as compared to the equivalent solid plate ones. The effects of the plate can also be seen in the zeroth and higher harmonic components, with the same trends as for the first harmonic components.

The corresponding non-dimensional vertical wave forces are given in Fig. 12. In contrast to the horizontal forces, the effects of the plate can be seen clearly at both deep and shallow drafts. At the deep draft, the peak of vertical forces with the plate appears earlier than the solitary cylinder. In the time series, the porous plate reduces the forces but also shifts the forces compared to the equivalent solid plate. Moreover, porosity tends to flatten the peaks in the vertical forces for both drafts. In general, the first harmonics of the vertical forces are significantly affected by the plates. Interestingly, the small heave plate ($D_d/D_c = 1.5$) decreases the first harmonic of the vertical forces compared to the solitary cylinder. The porous plate reduces all harmonics of the vertical forces compared to the equivalent solid plate.

5.1.2. Harmonic operators of horizontal wave forces

Fig. 13 shows the amplitude of the first-, and second-harmonic components, as well as the mean value of horizontal wave forces at both the deep ($d/D_c = 2.2$) and shallow ($d/D_c = 0.7$) drafts. The measured horizontal forces exerted on the truncated cylinder without the plate (Model A), given in blue color, indicate a monotonic behavior with respect to wave frequency. Generally, wave steepness has minor effects on the non-dimensional horizontal forces compared to the influence of wave frequency. The measured forces are well-described by the first-, and second-order potential flow theory at both drafts.

The presence of the plate affects the first harmonic components. At deep draft, the plates slightly increase the horizontal forces compared to the solitary cylinder for $0.2 < \omega^2 D_c/g < 1.8$. In contrast, at the shallow draft, the forces increase significantly with increasing the diameter of the plate. Notably, significant wave steepness results in decreased forces for large heave plates at the frequency where non-dimensional wave forces are maximized. Therefore, potential flow theory tends to overestimate the forces when $H/\lambda > 0.02$. It is worth noting that the effect of heave plates is mitigated at high wave frequency where the wavelength is very short compared to the cylinder.

Similar to the first harmonics, the influence of the plate on the second harmonics and mean drift forces is not important at the deep draft. However, at the shallow draft, the plate has also a dominant impact on the second harmonics and the mean of the horizontal forces. Significant peaks are measured around $\omega^2 D_c/g = 0.8$ for the second harmonic horizontal forces at the shallow draft for Model C and E. The peaks increase with increasing the plate diameter and decrease with increasing the wave steepness. The potential flow method predicts the general tendency well, but the magnitude is overestimated around peak frequency. Furthermore, the plates at the shallow draft strongly affect the horizontal mean drift forces, while there is almost no difference at the deep draft. Increasing the plate size leads to an increase in the mean horizontal force, particularly at the peak frequency ($\omega^2 D_c/g \approx 1.2$). On the other hand, the porosity of the plate has a negligible effect on the mean horizontal force.

However, the perforated plate (Model D), shown in orange, reduces the first and second harmonics of the horizontal forces compared to the equivalent solid plate (Model C) shown in green. The reduction is more visible at the shallow draft: for wave frequency $\omega^2 D_c/g = 1.2$, porosity decreases the load by approximately 30%. The potential flow describes well, in general, the first harmonics of the experimental measurements with the porous parameter ($\kappa = 5$) in Darcy's law to represent the porosity factor $\tau = 10\%$.

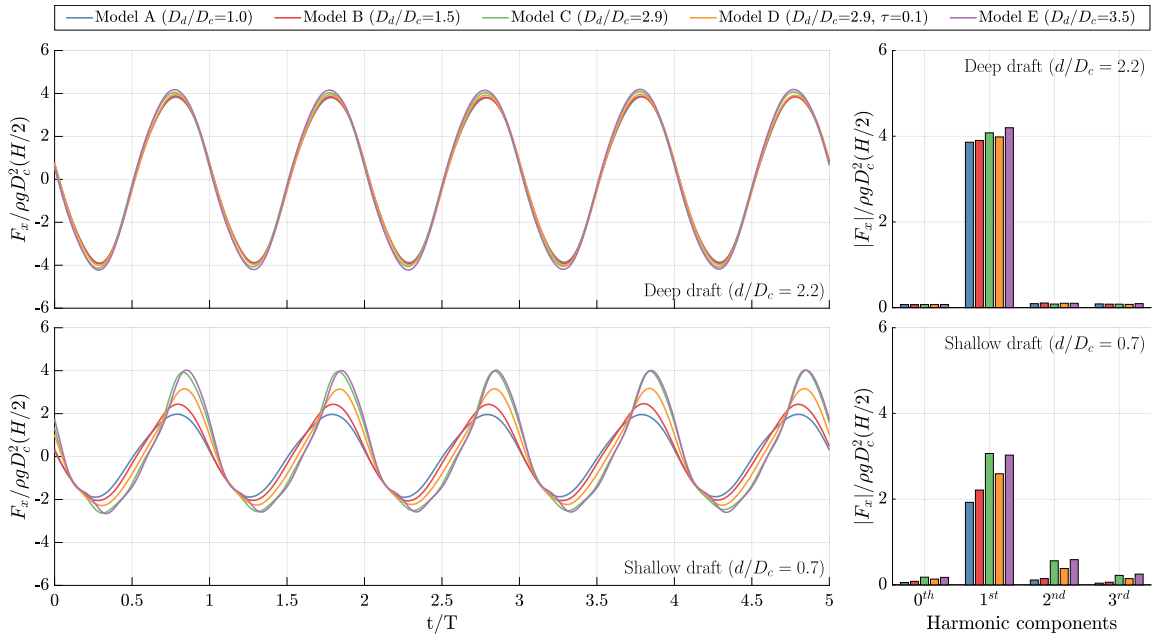

Fig. 11. Non-dimensional horizontal wave forces at deep (top) and shallow (bottom) drafts at the non-dimensional wave frequency ($\omega^2 D_c/g = 1.0$) with wave steepness ($H/\lambda = 0.06$).

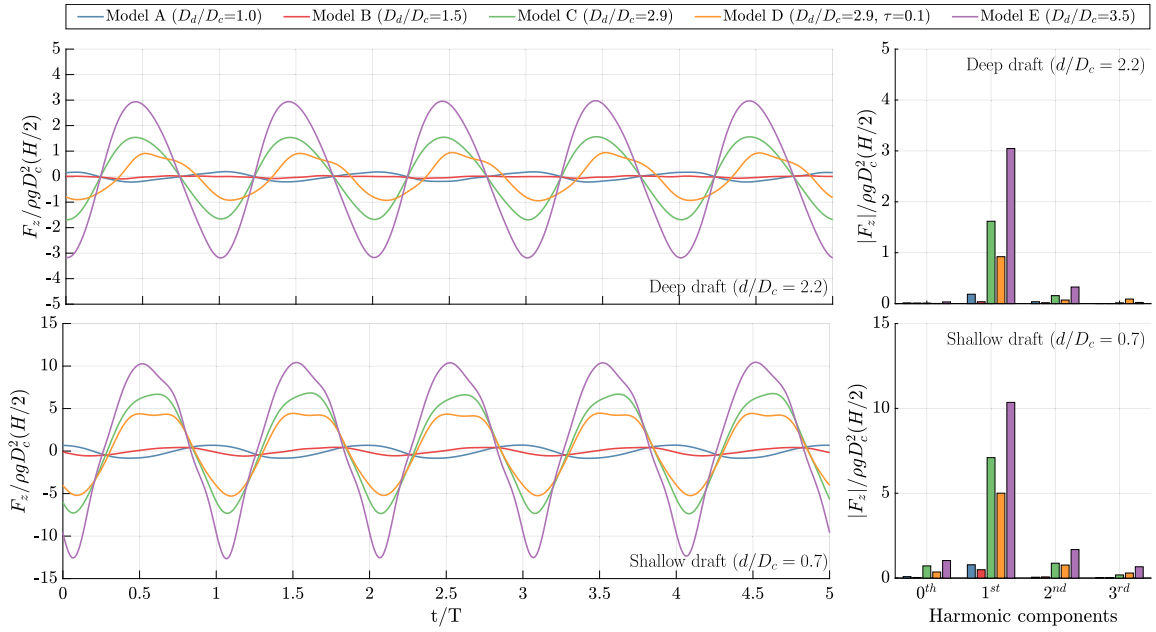

Fig. 12. Non-dimensional vertical wave forces at deep (top) and shallow (bottom) drafts at the non-dimensional wave frequency ($\omega^2 D_c/g = 1.0$) with wave steepness ($H/\lambda = 0.06$).

5.1.3. Harmonic operators of vertical wave forces

The measured harmonics of the vertical wave loads are summarized as the harmonic operators in Fig. 14. The first harmonics are monotonically decreasing with increasing wave frequency on the solitary cylinder (Model A) at the deep and shallow drafts. As the wave frequency increases, the forces decrease and converge to zero. This is because the vertical forces are exerted only on the bottom of the cylinder. The water particle velocity decreases exponentially and cannot influence the cylinder bottom at high frequency. However, at low frequency, the non-dimensional vertical forces reach around 0.8 ($F_z^{(\omega)}/\rho g A_w(H/2) = 1$) dominated by incident wave forces known as Froude–Krylov forces.

On the other hand, with the heave plate, the vertical forces not only act on the bottom but also on the top of the plate. As a result, the amplitude of the first harmonic on the small plate (Model B) is lower than that of the solitary cylinder (Model A) at both drafts. In addition, with the large heave plates (Model C, D, and E), the first harmonics of the vertical forces are significantly increased in high-frequency regions. The forces decrease as the wave frequency decreases in low-frequency regions.

Interestingly, the potential flow theory indicates that the vertical forces are canceled out in these frequency regions, where the forces on the bottom and top of the plate are equal. However, the theory underestimates the forces compared to the experimental measurements around the cancellation frequency. The underestimation of the first harmonic of the vertical forces is more significant with higher wave steepness (H/λ) with the large heave plates. The wave steepness effects are dominantly visible in the low-frequency region with the solid plate.

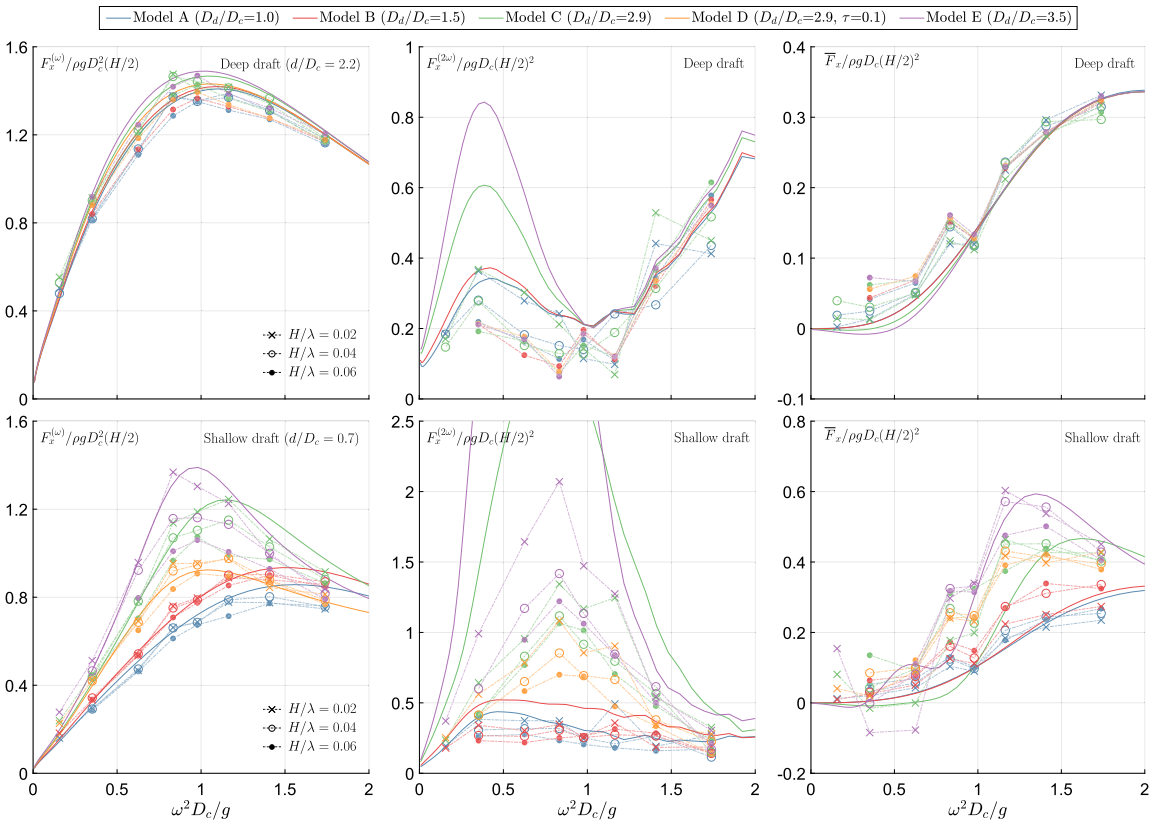

Fig. 13. Non-dimensional horizontal wave forces at deep (top) and shallow (bottom) drafts (×: $H/\lambda = 0.02$, ○: $H/\lambda = 0.04$, •: $H/\lambda = 0.06$, and −: HydroStar). Note that only 0.02 of wave steepness was tested for heave plates (Model B, D and E) at the deep draft ($d/D_c = 2.2$).

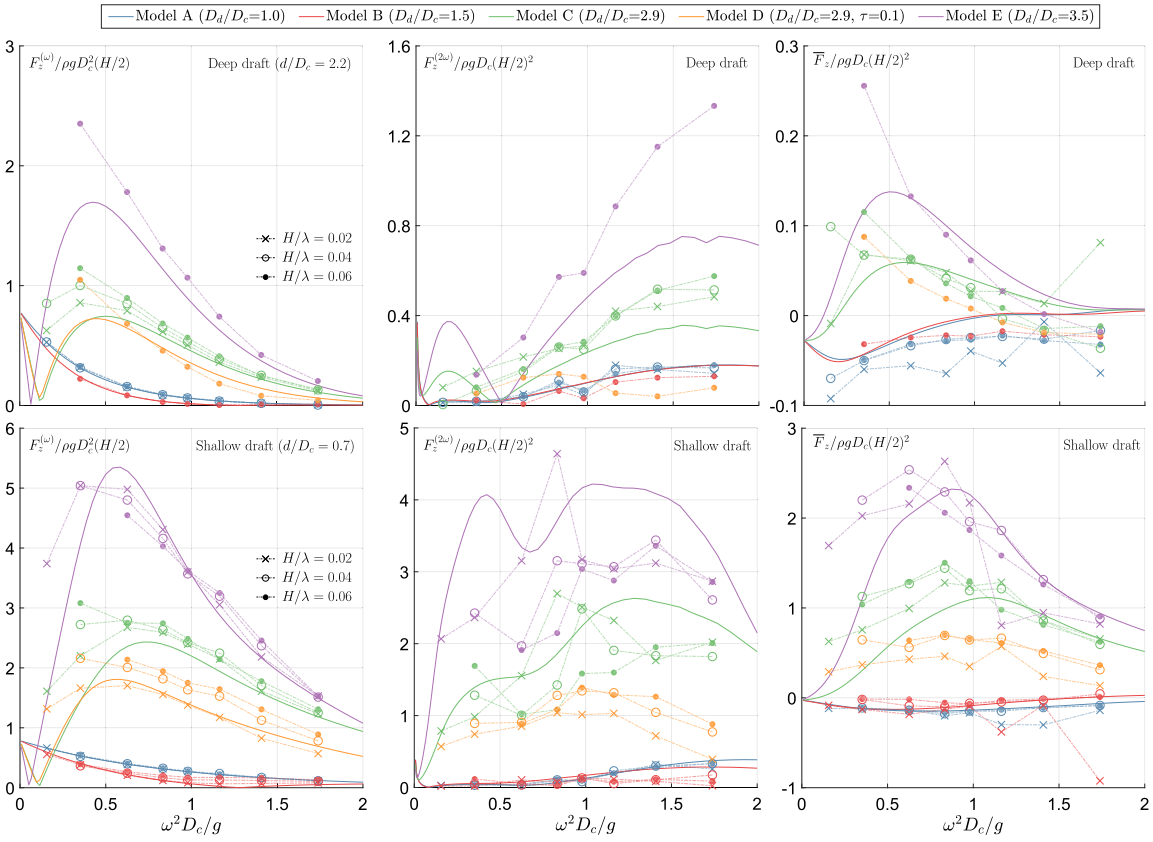

Fig. 14. Non-dimensional vertical wave forces at deep (top) and shallow (bottom) drafts (×: $H/\lambda = 0.02$, ○: $H/\lambda = 0.04$, •: $H/\lambda = 0.06$, and −: HydroStar). Note that only 0.02 of wave steepness was tested for heave plates (Model B, D and E) at the deep draft ($d/D_c = 2.2$).

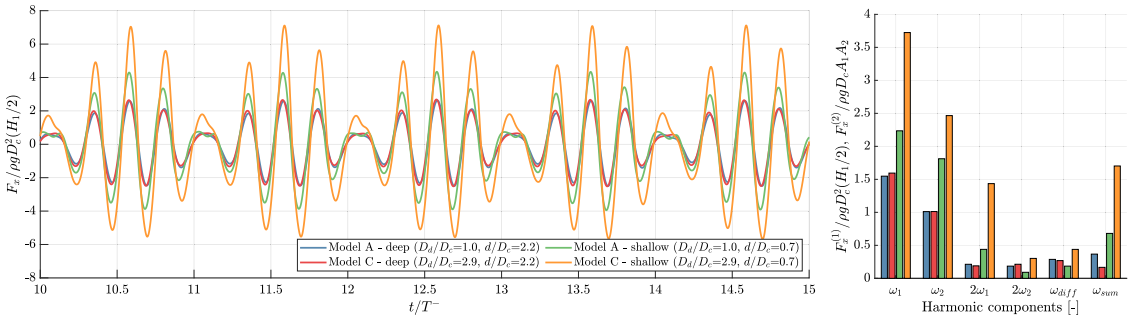

(a) Time series of horizontal wave forces in bichromatic waves (b) Harmonics

Fig. 15. Non-dimensional horizontal wave forces on the truncated circular cylinder without (D_d/D_c = 1.0) and with the heave plate (D_d/D_c = 2.9) in bichromatic waves ($\omega_1^2 D_c/g = 0.83$ and $\omega_2^2 D_c/g = 1.30$) at deep and shallow drafts.

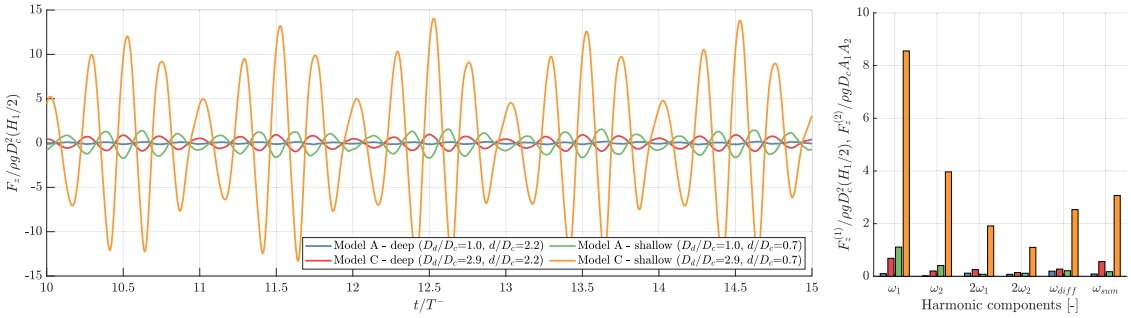

(a) Time series of vertical wave forces in bichromatic waves (b) Harmonics

Fig. 16. Non-dimensional vertical wave forces on the truncated circular cylinder without (D_d/D_c = 1.0) and with the heave plate (D_d/D_c = 2.9) in bichromatic waves ($\omega_1^2 D_c/g = 0.83$ and $\omega_2^2 D_c/g = 1.30$) at deep and shallow drafts.

Whereas it is much less significant in the high frequency ($\omega^2 D_c/g > 1$). Further discussion of the first harmonic of vertical wave forces is provided in Section 6.

For the porous plate, the effects are visible in the whole frequency range by decreasing the vertical forces, notably at the shallow draft. The potential flow theory is generally aligned with the experimental measurement, especially with the lower wave steepness ($H/\lambda = 0.02$). The first harmonic on the porous plate (Model D, $\tau = 0.1$) is predicted well by Darcy's law with the porous parameter ($\kappa = 5$), especially for the lower wave steepness ($H/\lambda = 0.02$). However, significant differences exist in low-frequency regions.

The presence of a heave plate tends to increase the second-harmonic components at deep and shallow drafts, largely for the larger plates. The second harmonics of the vertical forces at the deep draft generally increase with respect to the frequency. At the shallow draft, on the other hand, only the cylinder alone and with a small heave plate show a similar trend as for the deep draft. With the larger plate, the second harmonics show fluctuations with respect to the frequency. The second-order theory predicts the general trend of the second-harmonic vertical forces. The porous plate reduces the second-harmonic vertical forces compared to the equivalent solid plate (Model C) at the deep and shallow drafts.

Lastly, the mean drift forces exerted on the solitary cylinder and the cylinder with the small plate (Model B) show negative forces at the deep and shallow drafts. With the large heave plates, the mean drift forces are increasing more significantly at the shallow draft. The porous plate decreases the mean forces by 50% compared to the equivalent solid plate at the shallow draft.

5.2. Wave loads in bichromatic waves

The horizontal and vertical wave forces acting on the cylinder without (Model A) and with heave plate (Model C) are examined at deep ($d/D_c = 2.2$) and shallow ($d/D_c = 0.7$) drafts in the bichromatic waves.

The harmonic amplitudes of the forces at $\omega_1, \omega_2, \omega^+, \omega^-$ are non-dimensionalized with,

$$F'^{(\omega_j)} = \frac{F^{(\omega_j)}}{\rho g D_c^2 A_j}, \qquad F'^{(\omega^{+,-})} = \frac{F^{(\omega^{+,-})}}{\rho g D_c A_1 A_2} \tag{8}$$

where ω_j represents the wave frequency components. A_1 and A_2 are the first harmonics of the wave amplitude corresponding to each wave frequency.

5.2.1. Time series and harmonic components

Figs. 15–16 show one example of wave-loads time series in bichromatic waves together with the amplitudes of first-, and second-harmonics of ω_1 and ω_2 as well as the sum- and difference-frequency components, ω^+ and ω^-. The amplitudes of the forces are obtained using the least-square method given in Eq. (6).

In the time series, it is clear that the behavior of horizontal forces presents envelopes repeated in T^-, regardless of the presence of the plate and the drafts. At the deep draft, the forces are almost the same without or with the plate. However, at the shallow draft, the forces are significantly influenced by the plate, resulting in an increased amplitude. On the other hand, the amplitude and the phase of vertical forces of Model C are increased and shifted compared to Model A in both drafts. This is consistent with the trend observed with monochromatic waves.

5.3. Harmonic operators of the first harmonics

Fig. 17 shows the first harmonics of horizontal and vertical wave forces in bichromatic waves represented by the symbols with the solid face colors. For comparison, the first harmonics from the monochromatic waves with the wave steepness of $H/\lambda = 0.02$ are plotted with

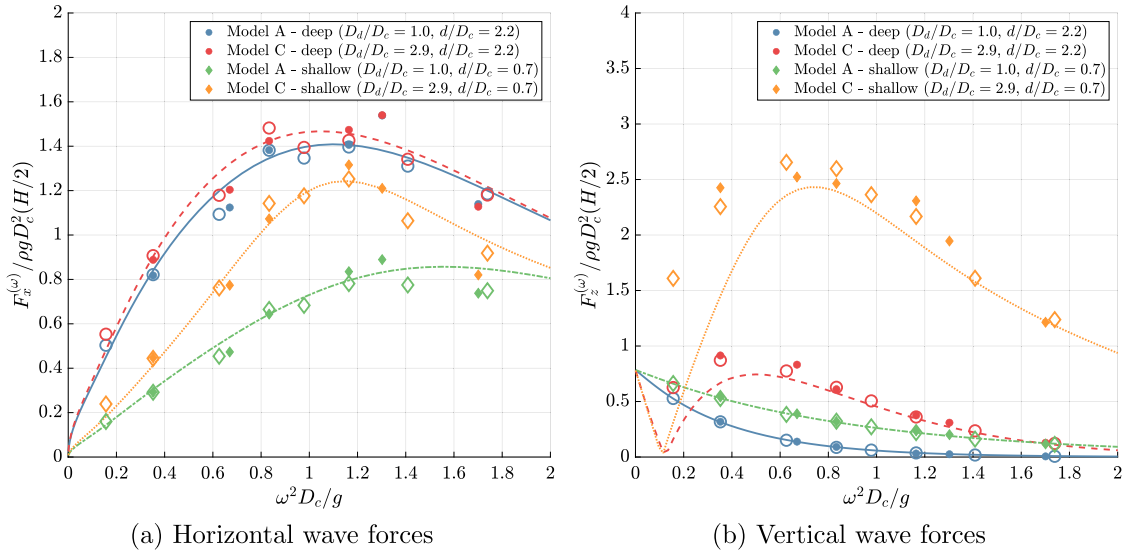

(a) Horizontal wave forces (b) Vertical wave forces

Fig. 17. First harmonic wave loads on the truncated circular cylinder with and without heave plate at deep and shallow drafts (lines: HydroStar, symbols without fill: monochromatic waves $H/\lambda = 0.02$, symbols with fill: bichromatic waves).

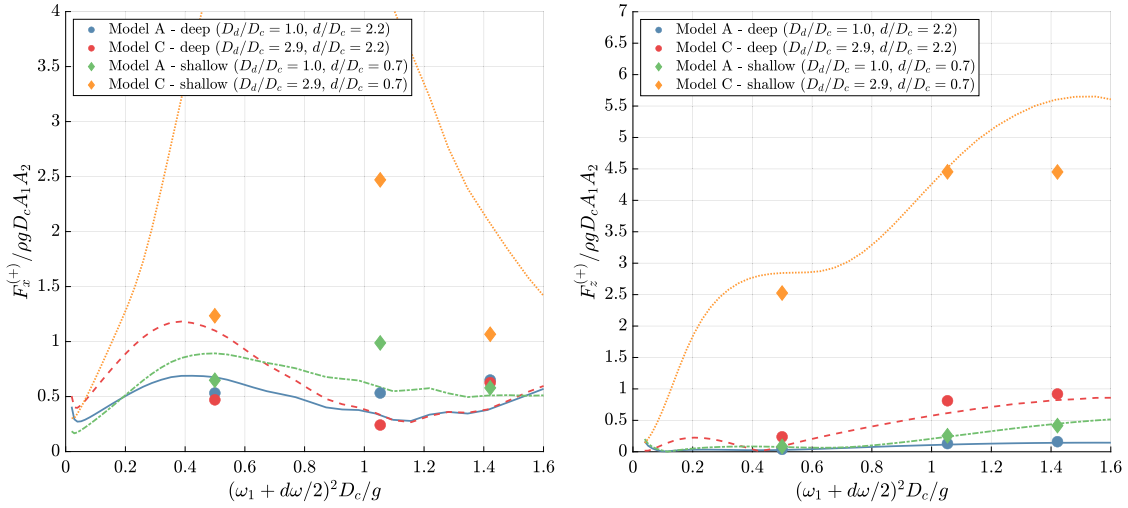

(a) Horizontal wave forces (b) Vertical wave forces

Fig. 18. Wave loads at sum frequency ω^+ on a truncated circular cylinder with and without heave plate at deep and shallow drafts in bichromatic waves (lines: HydroStar (near-field), symbols with colors: bichromatic waves).

symbols without face color. The first-order wave forces from potential flow theory are presented in solid lines with colors corresponding to the configuration and the drafts.

In bichromatic waves, the first harmonics of the forces are generally close to the measurements in monochromatic waves. As the frequency increases, the vertical forces on the solitary cylinder decrease and converge to zero. It is important to note that the vertical forces on the heave plate (Model C) are similar in magnitude to the regular wave ones at the low frequency, where the potential flow theory underestimates the forces.

5.3.1. Sum- and difference-frequency components

Wave loads at the sum and difference frequencies in bichromatic waves are shown with the symbols in Figs. 18–19. The second-order sum- and difference-frequency wave forces evaluated by QTFs using HydroStar are given in solid lines for comparison. Similar to the second harmonic in the monochromatic waves, the horizontal forces are less affected by the presence of the plate at the deep draft but significantly affected at the shallow draft. The effect of the plate is noticeable on the vertical forces at both deep and shallow drafts.

In the difference-frequency components, the slowly varying forces on the solitary cylinder and cylinder with the plate are identical at the deep draft. The forces on the cylinder with the plate are significantly increased at the shallow draft, which is a similar tendency to the mean drift forces in monochromatic waves.

In general, the potential flow theory predicts well the horizontal and vertical wave forces at the sum and difference frequencies. However, the theory tends to overestimate the horizontal forces at sum frequency and underestimate the vertical forces at difference frequency. This is again similar to what was obtained for the second harmonic and mean of monochromatic waves, where the second-order horizontal forces were higher than those in the measured second harmonics, and the zeroth-order vertical forces were lower than the measurements in the low-frequency region.

6. Discussion

In the previous section, potential flow theory, commonly employed in engineering models, was seen to generally predict the wave loads at the 0th, 1st, and 2nd harmonics. However, there are differences

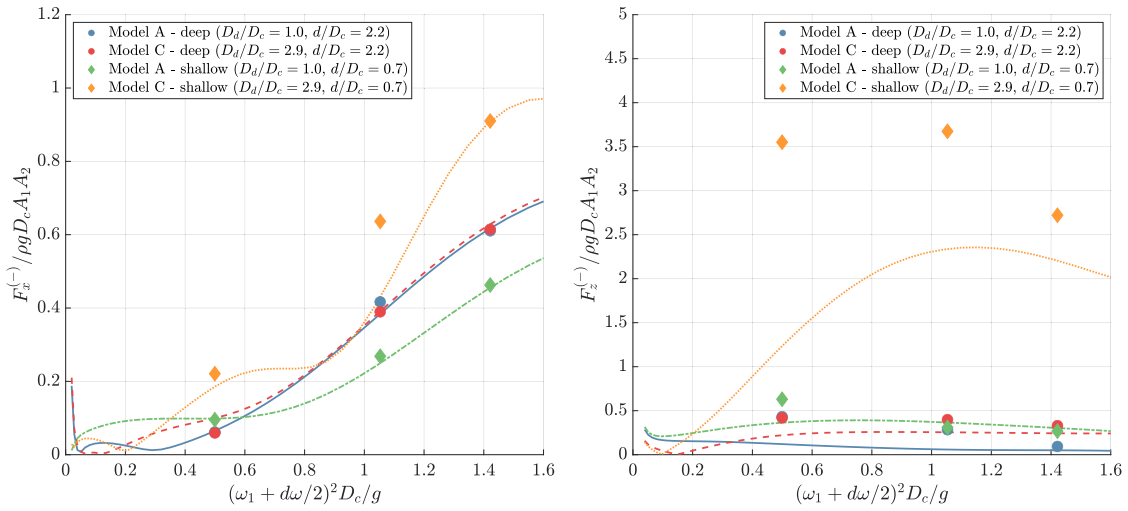

(a) Horizontal wave forces (b) Vertical wave forces

Fig. 19. Wave loads at difference frequency ω^- on a truncated circular cylinder with and without heave plate at deep and shallow drafts in bichromatic waves (lines: HydroStar (middle field), symbols with colors: bichromatic waves).

between the experimental measurements and theoretical predictions when the cylinder is equipped with the heave plate. Of particular interest is the underestimation of the first harmonics that dominate the wave loads. Therefore, the focus of this section is to provide a more detailed understanding of the first harmonic wave loads.

6.1. Wave loads on a vertical circular cylinder in literature

This section places the present experiments on a truncated vertical circular cylinder (Model A) within relevant experimental databases in the literature. The experimental databases available in the literature mainly concentrate on horizontal wave forces, with only limited discussion on vertical wave forces.

Fig. 20 illustrates the first harmonics of wave loads exerted on the vertical circular cylinder with respect to the non-dimensional wave frequency $\omega^2 D_c/g$. The cylinder configurations in the literature are represented by the draft ratio d/D_c. For instance, the present study considers two draft ratios: deep draft ($d/D_c = 2.2$) and shallow draft ($d/D_c = 0.7$). Previous studies examined the bottom-mounted cylinder ($d/D_c = 3.9$, Kristiansen and Faltinsen (2017)) and the truncated cylinder ($d/D_c = 1.5$, Sung et al. (2007) and $d/D_c = 3.0$, Boo (2006)).

For comparison, the potential flow theory on the bottom-mounted circular cylinder (McCamy and Fuchs, 1954) and on the truncated cylinder (Garrett, 1971) are presented in solid lines. In general, the first harmonic wave loads, non-dimensionalized as $F^{(\omega)}/\rho g D_c^2 (H/2)$, are described well by the linear potential flow theory, which evaluates the forces analytically.

The outcomes of the present experiment are consistent with the general trend in the literature. Increasing the draft ratio increases the non-dimensional horizontal forces. This can be attributed to the increase in the wetted body surface. Eventually, the horizontal forces acting on the truncated cylinder are close to those acting on the bottom-mounted cylinder. Conversely, decreasing the draft ratio leads to an increase in the non-dimensional vertical wave forces. As confirmed in Section 5, the vertical forces on the solitary cylinder decrease with increasing wave frequency and converge to zero.

6.2. Wave loads on a vertical circular cylinder with a heave plate

In this section, we focus on the underestimation of the first harmonic of the vertical wave forces in the low-frequency region, as observed in Section 5. To begin with, we investigate the flow field in regular waves by solving the incompressible Navier–Stokes equation with a CFD solver *foamStar*. The flow is visualized around the heave plate, where flow separation is expected. The vertical wave forces evaluated in the CFD are compared with the experimental measurements. Furthermore, attempts are made to overcome the underprediction of potential flow solutions by introducing the viscous drag term of Morrison's equation.

6.2.1. CFD simulations

The CFD simulations are carried out using the *foamStar* solver, which is an in-house library co-developed by Bureau Veritas and Ecole Centrale de Nantes. The library is based on the *interDymFoam* which is a standard multiphase solver in OpenFOAM. The detailed computational algorithms and applications of the solver are presented in Monroy et al. (2016), Choi et al. (2020), Kim (2022), Descamps (2023). The Volume of Fluid (VOF) method is used to capture the free surface in the two-phase flow. The regular waves are generated using *wave2Foam* with the free surface $k-\omega$ SST turbulence model as well as the Crank–Nicolson time integration scheme to minimize the wave dissipation during its propagation.

Spatial refinement is considered around the free surface as $\lambda/\Delta x = \lambda/\Delta y > 80$ and $H/\Delta z > 15$. Relaxation zones are taken with wavelength, λ, for the incoming waves, 2λ for wave reflections at the back of the domain, and 0.5λ on the side. In total, about 5 million cells are used with the symmetric computational domain. The time step dt is taken as $T/dt = 500$.

Fig. 21 presents the flow field with Model C ($D_d/D_c = 2.9$) in the regular waves ($\omega^2 D_c/g = 0.35$, $H/\lambda = 0.04$) at the deep draft. The magnitude of the flow velocity field is illustrated along with the vector of the flow. A strong flow separation is observed at the edge of the plate in CFD. This flow separation is not considered in the potential flow theory.

6.2.2. Engineering approximation of viscous forces using a Morison-type formulation

A simplified method is presented to investigate the effect of the vertical wave forces from flow separation. The contribution of the flow separation can be modeled using viscous drag forces from the Morison equation. The first-order vertical wave forces can be defined here as,

$$F_z^{(1)} = F_z^p + F_z^v \tag{9}$$

where F_z^p is the first-order hydrodynamic forces computed by the potential flow theory (Han et al., 2024) and F_z^v is the viscous drag force

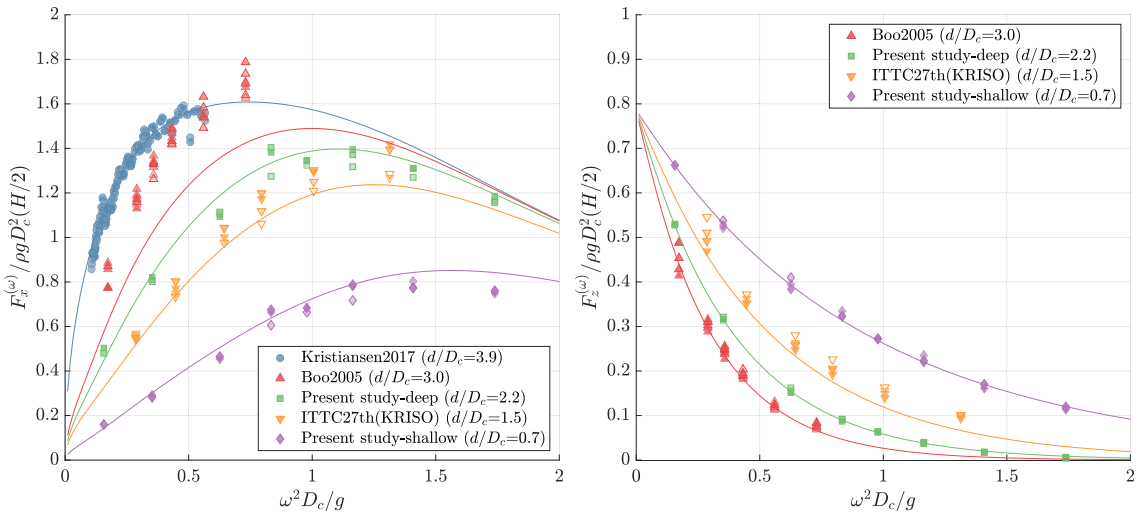

(a) Horizontal wave forces (b) Vertical wave forces

Fig. 20. Non-dimensional first harmonics of horizontal and vertical wave forces on a vertical circular cylinder. Lines are the results using the linear potential flow theory: (a) McCamy and Fuchs (1954) for a bottom-mounted cylinder and Garrett (1971) for a truncated cylinder. Symbols are the experimental measurements: (1) Kristiansen and Faltinsen (2017) for the bottom-mounted cylinder (○), (2) Boo (2006) (△), (3) ITTC 27th OEC (2014), Sung et al. (2007) (▽), and (4) the present study (□, ◇) for the truncated cylinder. The transparency of the face color means the wave steepness.

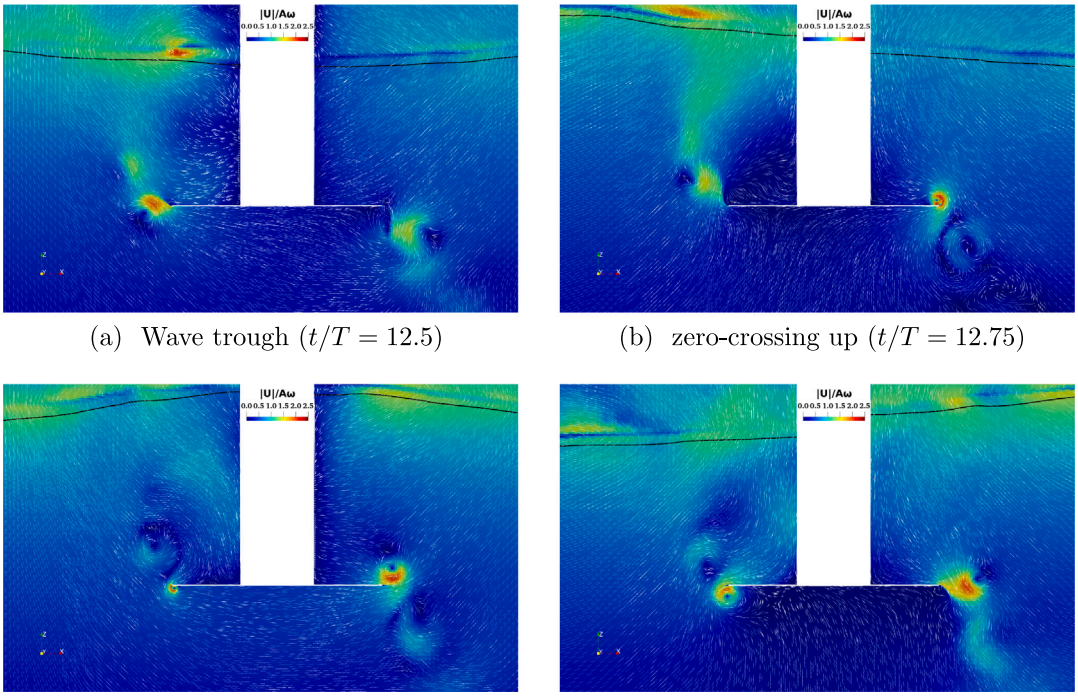

(a) Wave trough ($t/T = 12.5$) (b) zero-crossing up ($t/T = 12.75$)

(c) Wave crest ($t/T = 13.0$) (d) Zero-crossing down ($t/T = 13.25$)

Fig. 21. Magnitude of non-dimensional flow velocity ($|\mathbf{U}|/(H/2)\omega$) and free surface (black solid line) around the cylinder with the heave plate ($D_d/D_c = 2.9$) at the deep draft ($d/D_c = 2.2$) in the monochromatic waves ($\omega^2 D_c/g = 0.35$, $H/\lambda = 0.04$) propagating in positive x-axis (left to right).

from the Morison equation defined as

$$F^v = \frac{1}{2}\rho C_D S_d U_z |U_z| \tag{10}$$

where $S_d = 1/4\pi D_d^2$ is the plate's surface area and C_D stands for the drag coefficient.

The flow velocity U_z is computed using the linear velocity potential of the incident wave, ϕ_I,

$$U_z(t) = \frac{\partial \phi_I}{\partial z} = \Re\mathfrak{e}\left\{\frac{-igAk_0}{\omega}\frac{\sinh k_0(z+h)}{\cosh k_0 h}e^{i(k_0 x-\omega t)}\right\} \tag{11}$$

where the wave number k_0 is decided by using the linear dispersion relation, $\omega^2 = k_0\, g \tanh k_0 h$. The reference position is at the center of the submerged circular plate ($x = 0$, $z = -d$).

Fig. 22 shows an example of the vertical force time history on Model C in regular waves with the non-dimensional wave frequency ($\omega^2 D_c/g = 0.35$) and wave steepness ($H/\lambda = 0.04$) at the deep draft ($d/D_c = 2.2$). The drag coefficients on Model C ($D_d/D_c = 2.9$) are obtained iteratively by targeting the amplitude of the measured vertical forces, resulting in constant values of 17, 23, and 28 for the three wave steepnesses, respectively.

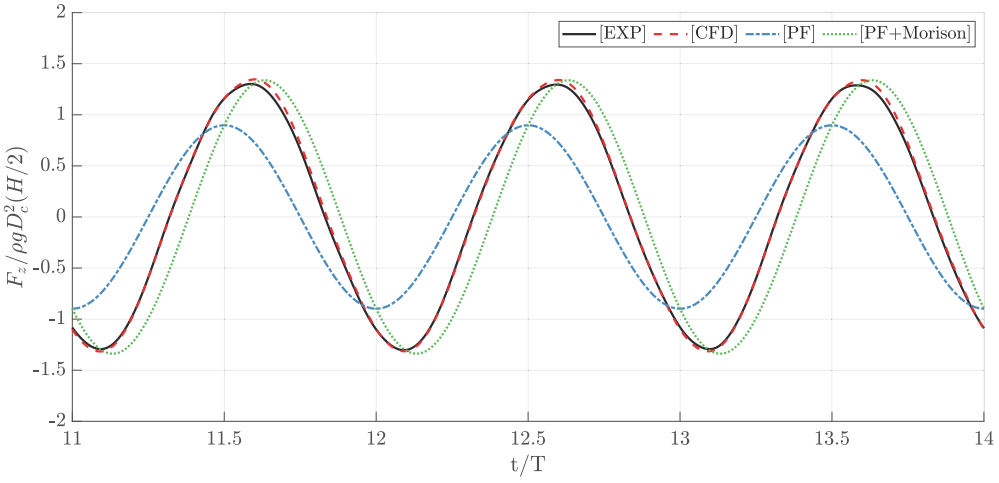

Fig. 22. Time series of non-dimensional vertical wave forces on the cylinder with the heave plate ($D_d/D_c = 2.9$) at the deep draft ($d/D_c = 2.2$) in the regular waves ($\omega^2 D_c/g = 0.35$, $H/\lambda = 0.04$): experiment (solid line), CFD (dashed line), potential flow theory (dashed-dot line), and simplified method with $C_D = 23.0$ (dotted line).

The CFD result is in very close agreement with the experiment, while the potential flow theory largely underestimates the amplitude and has a phase discrepancy. An important improvement of the potential flow prediction is obtained by including the viscous drag forces (Eq. (9)), but there is still some inconsistency in the phase.

There are two possible reasons for this difference. The first reason is a time lag due to the distribution of vortices, which has a certain inertia inducing a force not in phase with the excitation velocity. The second reason is the reference position of the flow velocity. The drag forces are related to the flow separation that occurs at the edge of the plate, which is far from the reference position. This aspect is left for future research focusing on engineering design models.

Fig. 23 shows the prediction of the first harmonic operator for vertical forces in three wave steepnesses using the simplified method, i.e. potential flow theory with added viscous drag and CFD. The CFD simulations accurately capture the vertical forces in that low-frequency region as well as the effects of wave steepness. Similarly, the simplified method predicts well the first harmonic amplitude over the entire frequency range using the constant drag coefficient corresponding to each wave steepness. It is worth noting that at the deep draft ($d/D_c = 2.2$), the drag coefficient depends on wave steepness and not frequency. The contribution of viscous drag forces appears in the low-frequency region ($\omega^2 D_C/g < 1.0$), and it is most significant at the cancellation frequency of about $\omega^2 D_c/g = 0.1$.

6.2.3. Vertical force regimes on a cylinder with a heave plate at the deep draft

This section examines the vertical wave forces based on the size of the heave plate. The CFD simulations, described in Section 6.2.1, are conducted with seven representative plate diameter ratios: $D_d/D_c = 1.0, 1.5, 2.0, 2.5, 2.9, 3.5, 4.0$. A single regular wave, with wave steepness $H/\lambda = 0.04$ and non-dimensional frequency $\omega^2 D_c/g = 0.35$, is considered where strong flow separation is observed. This study is limited to the deep draft, $d/D_c = 2.2$.

The drag coefficients for different plate diameter ratios are provided at the top of Fig. 24. The coefficients are determined using the simplified method described in Eqs. (9)–(11) with reference to the CFD results. The values are interpolated for diameter ratios ranging from 1.0 to 4.0. For small plates ($D_d/D_c \leq 1.5$), where the difference between the diffraction theory and CFD is negligible, the coefficients are set to zero. It is also noted that the coefficient is converged to a constant value for large plates ($D_d/D_c \geq 3.5$).

The simplified method provides global responses that correspond to the wave frequency as shown at the bottom of Fig. 24. From the results, three distinct force regimes can be identified:

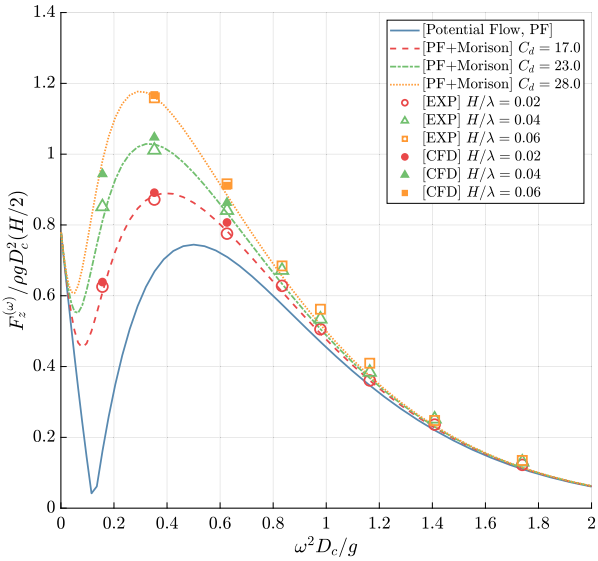

Fig. 23. Non-dimensional vertical wave forces on the cylinder with heave plate ($D_d/D_c = 2.9$) at the deep draft ($d/D_c = 2.2$): potential flow theory (solid lines), the potential flow theory with viscous drag (dashed, dashed-dot, and dotted lines), experiments (symbols with face colors), CFD (symbols without face colors).

- Region I: Diffraction. This region is governed by the potential flow theory. This is valid for the high-frequency region $\omega^2 D_c/g \geq 1.0$ for all plate diameters, and over the whole range of frequency for small heave plates with $D_d/D_c < 1.5$.
- Region II: Viscous drag. This is where viscous drag dominates, and the plate cancels out the hydrodynamic vertical forces in the linear potential flow theory ($0.1 \leq \omega^2 D_c/g \leq 0.5$).
- Region III: Diffraction + viscous drag. In this region, both potential and drag forces contribute to the vertical wave forces.

7. Conclusions

Wave loads on a fixed vertical and surface-piercing circular cylinder with a circular plate were investigated experimentally. The study examined five different plate configurations, including a perforated plate at deep and shallow submerged depths ($d/D_c = 2.2, 0.7$). The waves used in the experiment were monochromatic waves with three wave steepnesses ($H/\lambda = 0.02, 0.04, 0.06$) and bichromatic waves. The waves were carefully calibrated before testing.

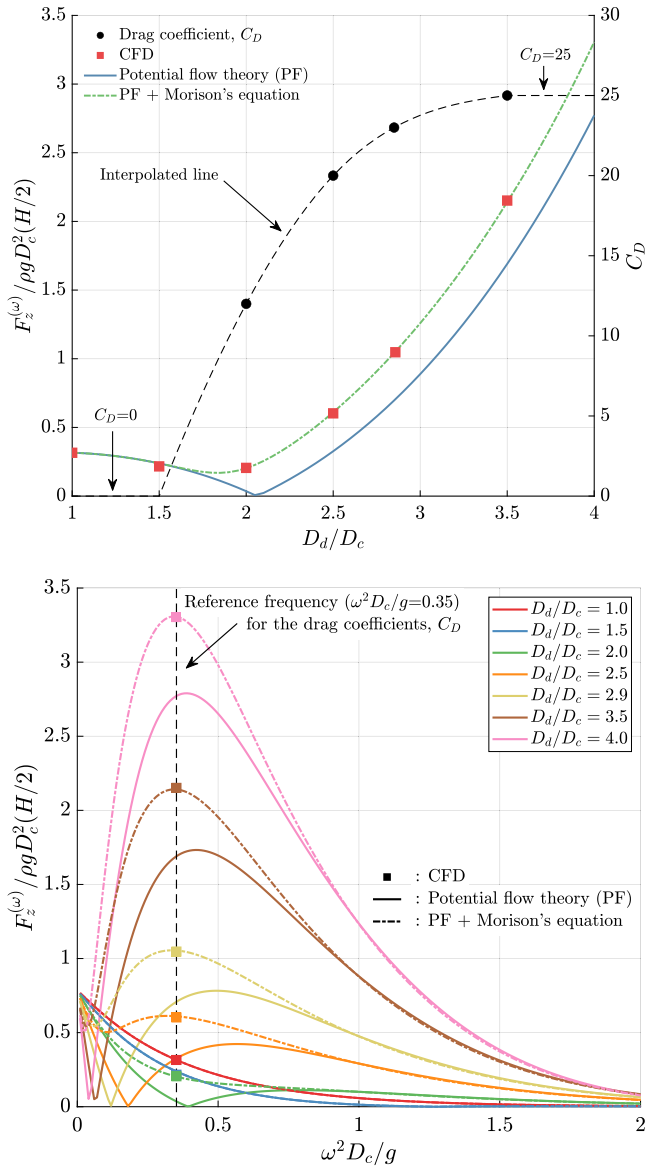

Fig. 24. Top: Determination of drag coefficients for diameter ratios D_d/D_c ranging from 1.0 to 4.0 with a reference frequency $\omega^2 D_c/g = 0.35$ and wave steepness $H/\lambda = 0.04$ at the deep draft $d/D_c = 2.2$. Bottom: Vertical wave excitation forces for non-dimensional wave frequency $\omega^2 D_c/g$ at the deep draft.

Horizontal and vertical wave forces exerted on the cylinder with the heave plate were of particular interest. A force transducer was used to measure wave loads, mitigating sources of error from wave reflection and structural responses. Measured force time histories were examined to provide insights into the influence of the plate diameter and submerged depth. Fourier analysis and least-squares fitting were utilized to obtain the harmonic content from the load time series induced by the monochromatic and bichromatic waves.

A boundary element method solver based on the potential flow theory (HydroStar) was used to evaluate the first- and second-order loads for comparison. Panel models for solid plates were made by considering the plate's thickness, and the source distribution method was used to solve a boundary integral equation. The perforated plate was modeled using Darcy's law by assuming a zero-thickness plate with a porous parameter, with a mixed approach (dipole + source methods).

In the present study, a significant effect of the heave plate was observed on the wave loads, particularly on the harmonic contents. The following outcomes can be highlighted:

- Heave plate diameter: The diameter ratio of the plate (D_d/D_c) significantly affects wave loads by altering the force amplitude and shifting the phase. The boundary element method used in this study provides reasonable agreement with the corresponding harmonics of experimental measurements. However, there are some inconsistencies observed in the harmonic content, particularly in the first harmonic of the vertical force. The BEM solver predicts the cancellation of first-order vertical forces in low-frequency regions but the experimental results show significant amounts of first-harmonic forces at these frequencies.
- Perforated plate: The perforated plate with 10% porosity effectively decreases the wave loads, which is more noticeable at the shallow draft. The panel method with porous parameter predicts well the first harmonic of the wave loads at the deep and shallow drafts.
- Wave steepness: The non-dimensional horizontal forces tend to decrease as the wave steepness increases. This trend is more pronounced for the large plates ($D_d/D_c = 2.9, 3.5$), whereas it is negligible for the solitary cylinder. On the other hand, the first harmonic of vertical forces with the large plates increases with increasing wave steepness in low-frequency regions.
- Submerged depth: The effect of the submerged depth is closely related to the wave steepness, as there is an interaction between the plate and the free surface. At the deep draft, horizontal forces are less affected by the heave plate and the wave steepness, but at the shallow draft, it becomes significant.
- Nonlinear loads: Mean drift and second harmonic loads, corresponding to the second-order loads, are found to be more pronounced at the shallow draft and clearly distinguished with respect to the plate-to-column diameter ratio (D_d/D_c). This finding emphasizes the importance of analyzing the higher-order loads, which anticipate inducing significant mooring tensions or structural vibrations when the floating body is equipped with heave plates near the free surface.

Further investigation of the first harmonics of wave loads was carried out. The results from the present experiment on the solitary cylinder ($D_d/D_c = 1.0$) were found to be consistent with the general trends in the literature.

CFD simulations were carried out to investigate the vertical forces on the heave plate ($D_d/D_c = 2.9$) at low wave frequency, for which the potential flow solver did not predict well the experimental result. It was observed that flow separation occurred around the edge of the plate. A simplified viscous approach using Morison's equation was used to model the contribution of the flow separation. The drag coefficient of Morison's equation was determined using experimental and numerical (CFD) results for the desired wave steepness at low frequencies where viscous drag is dominant. This approach permitted to provide an accurate prediction of the first harmonic vertical force amplitude compared to the experiment despite some remaining inconsistencies in the phase of the time series. In conclusion, a classification of vertical force regimes on the vertical circular cylinder with the heave plate, considering the constraints of the thin plate and deep draft condition.

CRediT authorship contribution statement

Seung-Yoon Han: Writing – review & editing, Writing – original draft, Visualization, Validation, Software, Methodology, Investigation, Formal analysis, Data curation, Conceptualization. **Benjamin Bouscasse:** Writing – review & editing, Supervision, Software, Project administration, Methodology, Investigation, Funding acquisition, Conceptualization. **Vincent Leroy:** Writing – review & editing, Supervision, Software, Methodology, Investigation, Conceptualization. **Sylvain Delacroix:** Writing – review & editing, Software, Investigation, Formal analysis. **Félicien Bonnefoy:** Writing – review & editing, Software, Investigation. **Erin E. Bachynski-Polić:** Writing – review & editing, Supervision, Methodology. **David Le Touzé:** Writing – review & editing, Supervision, Project administration, Funding acquisition, Conceptualization.

Declaration of competing interest

The authors declare that they have no known competing financial interests or personal relationships that could have appeared to influence the work reported in this paper.

Acknowledgments

This research is part of FLOAWER (FLOAting Wind Energy netwoRK) project. This project has received funding from the European Union's Horizon 2020 research and innovation programme under the Marie Sklodowska-Curie grant agreement N° 860879. This work was also carried out within the HP_Flow project in the WEAMEC framework, West Atlantic Marine Energy Community, and with funding from the Pays de la Loire Region (France) and European Regional Development Fund. The work presented in this paper was supported by Centrale Nantes - Bureau Veritas research chair. The authors acknowledge the tank testing team of LHEEA for their enthusiastic support of the experiment and Prof. Young-Myung Choi and Dr. Youngjun Kim from MASELA laboratory of Pusan National University for sharing computing resources.

Appendix A. Supplementary data

Supplementary material related to this article can be found online at https://doi.org/10.1016/j.oceaneng.2024.118970.

References

Boo, S., 2006. Measurements of higher harmonic wave forces on a vertical truncated circular cylinder. Ocean Eng. 33 (2), 219–233. http://dx.doi.org/10.1016/j.oceaneng.2005.03.006.

Bureau Veritas, 2020. HydroStar for Experts User Manual, Version 8.10. Technical Report, Bureau Veritas.

Chakrabarti, S.K., 1987. Hydrodynamics of Offshore Structures. WIT Press.

Chen, X.B., 2007. Middle-field formulation for the computation of wave-drift loads. J. Engrg. Math. 59 (1), 61–82. http://dx.doi.org/10.1007/s10665-006-9074-x.

Choi, Y.M., Kim, Y.J., Bouscasse, B., Seng, S., Gentaz, L., Ferrant, P., 2020. Performance of different techniques of generation and absorption of free-surface waves in Computational Fluid Dynamics. Ocean Eng. 214, 107575. http://dx.doi.org/10.1016/j.oceaneng.2020.107575.

Choisnet, T., Geschier, B., Vetrano, G., 2016. Initial comparison of concrete and steel hulls in the case of Ideol's square ring floating substructure. In: The 15th World Wind Energy Conference and Exhibition. Tokyo.

Chwang, A.T., 1983. A porous-wavemaker theory. J. Fluid Mech. 132, 395–406. http://dx.doi.org/10.1017/S0022112083001676.

Descamps, T., 2023. Numerical Analysis and Development of Accurate Models in a CFD Solver Dedicated to Naval Applications with Waves (Ph.D. thesis). Ecole Centrale de Nantes.

DNV-RP-C205, 2010. Environmental Conditions and Environmental Loads. Technical Report.

Faltinsen, O.M., Newman, J.N., Vinje, T., 1995. Nonlinear wave loads on a slender vertical cylinder. J. Fluid Mech. 289, 179–198. http://dx.doi.org/10.1017/S0022112095001297.

Fonseca, N., Nybø, S., Rodrigues, J.M., Gallego, A., Garrido, C., 2022. Identification of wave drift forces on a floating wind turbine sub-structure with heave plates and comparison with predictions. In: Volume 8: Ocean Renewable Energy. American Society of Mechanical Engineers, http://dx.doi.org/10.1115/OMAE2022-81467.

Fonseca, N., Pessoa, J., Mavrakos, S., Le Boulluec, M., 2011. Experimental and numerical investigation of the slowly varying wave exciting drift forces on a restrained body in bi-chromatic waves. Ocean Eng. 38 (17–18), 2000–2014. http://dx.doi.org/10.1016/j.oceaneng.2011.09.017.

Garrett, C.J.R., 1971. Wave forces on a circular dock. J. Fluid Mech. 46 (1), 129–139. http://dx.doi.org/10.1017/S0022112071000430.

Han, S.-Y., Bouscasse, B., Leroy, V., Le Touzé, D., 2024. Linear diffraction and radiation theory of water waves by a truncated vertical circular cylinder with heave plate in deep and shallow drafts. Int. J. Naval Archit. Ocean Eng. 100580. http://dx.doi.org/10.1016/j.ijnaoe.2023.100580.

ITTC, 2002. 7.6-02-09, ITTC-Recommended Procedures and Guidelines: Calibration of Load Cells. ITTC.

ITTC 27th OEC, 2014. Final Report and Recommendations to the 27th ITTC. ITTC 27th OEC.

Kim, Y.J., 2022. Numerical Improvement and Validation of a Naval Hydrodynamics CFD Solver in View of Performing Fast and Accurate Simulation of Complex Ship-Wave Interaction (Ph.D. thesis). Ecole Centrale de Nantes.

Kim, M.H., Yue, D.K.P., 1989. The complete second-order diffraction solution for an axisymmetric body Part 1. Monochromatic incident waves. J. Fluid Mech. 200, 235–264. http://dx.doi.org/10.1017/S0022112089000649.

Kim, M.H., Yue, D.K.P., 1990. The complete second-order diffraction solution for an axisymmetric body Part 2. Bichromatic incident waves and body motions. J. Fluid Mech. 211, 557–593. http://dx.doi.org/10.1017/S0022112090001690.

Kristiansen, T., Faltinsen, O.M., 2017. Higher harmonic wave loads on a vertical cylinder in finite water depth. J. Fluid Mech. 833, 773–805. http://dx.doi.org/10.1017/jfm.2017.702.

Li, H., Bachynski-Polić, E.E., 2021. Analysis of difference-frequency wave loads and quadratic transfer functions on a restrained semi-submersible floating wind turbine. Ocean Eng. 232, 109165. http://dx.doi.org/10.1016/j.oceaneng.2021.109165.

Lopez-Pavon, C., Watai, R.A., Ruggeri, F., Simos, A.N., Souto-Iglesias, A., 2015. Influence of wave induced second-order forces in semisubmersible FOWT mooring design. J. Offshore Mech. Arct. Eng. 137 (3), http://dx.doi.org/10.1115/1.4030241.

Malenica, S., Molin, B., 1995. Third-harmonic wave diffraction by a vertical cylinder. J. Fluid Mech. 302, 203–229. http://dx.doi.org/10.1017/S0022112095004071.

Maruo, H., 1960. The drift of a body floating on waves. J. Ship Res. 4 (3), 1–11.

Mavrakos, S.A., Grigoropoulos, 1994. Numerical and experimental investigation of the exciting wave loads on a vertical truncated cylinder. WIT Trans. Ecol. Environ..

McCamy, R.C., Fuchs, R.A., 1954. Wave forces on piles: a diffraction theory. Tech. Memo No. 69, Beach Erosion Board, U.S. Army Corps of Engineers.

Molin, B., 2023. Offshore Structure Hydrodynamics. Cambridge University Press, http://dx.doi.org/10.1017/9781009198059.

Monroy, C., Seng, S., Malenica, S., 2016. Développements et validation de l'outil CFD OpenFOAM pour le calcul de tenue à la mer. In: Conference: 15Èmes Journées de L'Hydrodynamique.

Newman, J.N., 1967. The drift force and moment on ships in waves. J. Ship Res. 11 (01), 51–60. http://dx.doi.org/10.5957/jsr.1967.11.1.51.

Pegalajar-Jurado, A., Bredmose, H., Borg, M., Straume, J.G., Landbø, T., Andersen, H.S., Yu, W., Müller, K., Lemmer, F., 2018. State-of-the-art model for the LIFES50+ OO-Star Wind Floater Semi 10MW floating wind turbine. J. Phys. Conf. Ser. 1104, 012024. http://dx.doi.org/10.1088/1742-6596/1104/1/012024.

Pinkster, J., Van Oortmerssen, G., 1978. Computation of the first and second order wave forces on oscillating bodies in regular waves. In: The 2nd International Conference on Numerical Ship Hydrodynamics.

Robertson, A.N., Gueydon, S., Bachynski, E., Wang, L., Jonkman, J., Alarcón, D., Amet, E., Beardsell, A., Bonnet, P., Boudet, B., Brun, C., Chen, Z., Féron, M., Forbush, D., Galinos, C., Galvan, J., Gilbert, P., Gómez, J., Harnois, V., Haudin, F., Hu, Z., Dreff, J.L., Leimeister, M., Lemmer, F., Li, H., Mckinnon, G., Mendikoa, I., Moghtadaei, A., Netzband, S., Oh, S., Pegalajar-Jurado, A., Nguyen, M.Q., Ruehl, K., Schünemann, P., Shi, W., Shin, H., Si, Y., Surmont, F., Trubat, P., Qwist, J., Wohlfahrt-Laymann, S., 2020. OC6 Phase I: Investigating the underprediction of low-frequency hydrodynamic loads and responses of a floating wind turbine. J. Phys. Conf. Ser. 1618 (3), 032033. http://dx.doi.org/10.1088/1742-6596/1618/3/032033.

Robertson, A., Wang, L., 2021. OC6 Phase Ib: Floating Wind Component Experiment for Difference-Frequency Hydrodynamic Load Validation. Energies 14 (19), 6417. http://dx.doi.org/10.3390/en14196417.

Robertson, A.N., Wendt, F., Jonkman, J.M., Popko, W., Dagher, H., Gueydon, S., Qvist, J., Vittori, F., Azcona, J., Uzunoglu, E., Soares, C.G., Harries, R., Yde, A., Galinos, C., Hermans, K., de Vaal, J.B., Bozonnet, P., Bouy, L., Bayati, I., Bergua, R., Galvan, J., Mendikoa, I., Sanchez, C.B., Shin, H., Oh, S., Molins, C., Debruyne, Y., 2017. OC5 Project Phase II: Validation of Global Loads of the DeepCwind Floating Semisubmersible Wind Turbine. Energy Procedia 137, 38–57. http://dx.doi.org/10.1016/j.egypro.2017.10.333.

Roddier, D., Cermelli, C., Aubault, A., Weinstein, A., 2010. WindFloat: A floating foundation for offshore wind turbines. J. Renew. Sustain. Energy 2 (3), http://dx.doi.org/10.1063/1.3435339.

Simos, A.N., Ruggeri, F., Watai, R.A., Souto-Iglesias, A., Lopez-Pavon, C., 2018. Slow-drift of a floating wind turbine: An assessment of frequency-domain methods based on model tests. Renew. Energy 116, 133–154. http://dx.doi.org/10.1016/j.renene.2017.09.059.

Sung, H., Kim, Y.S., Nam, B.W., Hong, S.Y., 2007. Experimental investigation of wave loads on a truncated vertical circular cylinder. In: The Korean Society of Ocean Engineering Conference.

Tao, L., Thiagarajan, K., 2003a. Low KC flow regimes of oscillating sharp edges I. Vortex shedding observation. Appl. Ocean Res. 25 (1), 21–35. http://dx.doi.org/10.1016/S0141-1187(03)00031-2.

Tao, L., Thiagarajan, K., 2003b. Low KC flow regimes of oscillating sharp edges. II. Hydrodynamic forces. Appl. Ocean Res. 25 (2), 53–62. http://dx.doi.org/10.1016/S0141-1187(03)00046-4.